DEVELOPMENT OF A FIBER-BASED, OPTOFLUIDIC SYSTEM FOR BIOANALYSIS

TANZIL KHAN

ROYAL INSTITUTE
OF TECHNOLOGY

Master of Science Thesis

Laser Physics
Department of Applied Physics
KTH – Royal Institute of Technology
Stockholm, Sweden 2010

ISBN: TRITA-FYS 2010:60
ISSN: 0280-316X
ISRN: KTH/FYS/--10:60--SE

Printed by Universitetsservice US AB, Stockholm 2010

Abstract

Optofluidics is a multidisciplinary field consisting of engineering, physics, chemistry, microtechnology and biotechnology; integrating microfluidics with optical technology. The implementation of optics with microfluidics not only enables denser integration but also allows the freedom to reconfigure which often is essential for manipulating and handling biological samples.

Our setup is based on a special optical fiber, which offers detection and flow integration in the same unit. In comparison to other optofluidic systems, it has the potential to give better optic and fluidic coupling, detection sensitivity, and versatility. Not much work has been performed with this kind of setup previously, thus, a lot of developing efforts were invested into instrumental development involving, e.g., different fabrication methods, lasers, optical fibers, capillaries, photomultiplier tubes (PMT) and filters. The challenge of having detection and flow in the same fiber is that the fiber often has to have openings (for fluidic access) to allow for a continuous flow in the hollow axial part (capillary). The two-hole fiber (THF) used in this work fits this criterion except for the need to access the capillary via in the fused silica fiber wall. Several fabrication methods were applied to make holes in the fiber involving; grinding, diamond blade sawing, hydrofluoric (HF) acid etching and tesla spark coil ablation. In this context, an important issue lies in obtaining a smooth fabricated hole via clean from debris.

In order to obtain high fluorescence detection sensitivity, it is very important to choose the right fiber and filter combination. Initially, each filter was tested to determine the transmission and then different filter combinations were tried to optimize the signal-to-noise ratio (SNR). Additionally, a carbon-coated optical fiber was chosen to simultaneously guide the excitation and emission radiation, since the carbon layer can absorb the remnant light, which is coming from the environment or from the cladding. The test of the detection system was performed in three stages. The first stage involved a common standard fluorescent dye used as a simple way to determine the limit of detection (LOD). The second stage involved fluorescent beads. These beads are commonly used, e.g., in microcopy, for determining if a setup can detect biological components. The third stage involved a live cell application using E-coli bacteria, which had been transfected with enhanced green fluorescent protein (EGFP).

The detection of fluorescent beads and EGFP were achieved. We have found the best method to fabricate the fiber holes and have observed different ways of improving the apparatus further. There are challenges still ahead such as detecting individual EGFP and improving the LOD even further.

Acknowledgments

I would like to thank Fredrik Laurell and Mårten Stjernström for giving me the opportunity to do my diploma work at the Laser Physics department. Mårten Stjernström has introduced me to optofluidics giving me great insight and guidance. I cannot thank you enough! You have shown me such a great deal, shared your knowledge and wisdom.

Walter Margulis and Oleksandr Tarasenko from Acreo has helped us by providing the fibers, the fusion parameters and for grinding the fibers to obtain access holes. The knowledge and materials were greatly appreciated. Aman Russom from Cell Physics department at KTH has provided us with EGFP bacteria, which has helped test our setup. I would like to thank the whole Laser Physics group for helping me with various questions and giving me ideas. I would also thank Jens Tellefsen for having critically read the entire manuscript.

It was fun playing floor ball with the people from the Laser Physics department and I will surely miss that.

Contents

Glossary of Terms and Abbreviations

CW	Continuous Wave
DPSSL	Diode-Pumped Solid-State Laser
EDL	Electrical Double Layer
EOF	Electroosmotic Flow
EGFP	Enhanced Green Fluorescent Protein
HF	Hydrofluoric
LIF	Laser-Induced Fluorescence
LOD	Limit of Detection
NA	Numerical Aperture
PMT	Photomultiplier Tube
SMF	Single-Mode Fiber
SNR	Signal-to-Noise Ratio
THF	Two-Hole Fiber
TIR	Total Internal Reflection

1 Introduction

Optofluidics is an interesting emerging research field integrating microfluidics with optical technology[1]. The realization of optofluidics can improve the overall system performance since it not only enables denser optics with microfluidic integration, but it also allows for high freedom of system reconfiguration, which often is essential for manipulating and handling biological samples.[2]

An interesting opportunity for sample detection in an optofluidic system is the potential to tightly integrate with it laser-induced fluorescence (LIF), due to its selectivity and extreme sensitivity. [3, 4] A low detection limit is thus achieved primarily as a result of the low divergence and good beam quality of the laser beam, that makes it easy to focus the light into nano-to-microliter volumes with an intense irradiation.[5, 6]

Microfluidics has shown great benefits, e.g., in DNA sequencing, enabling high throughput through parallelization[7]. Further applications can be found in chemical process monitoring, food safety, pharmaceutical production and research, environmental monitoring and homeland security. Additionally, groups working in drug research, have realized that the massive parallelization and throughput reduces the cost per acquired data point as well as significantly reducing the experiment time and sample consumption[8].

The optical network technology is already well established providing single-mode fibers (SMF), light sources and detection technologies with high quality, low-loss, modular means of generating, transporting and analyzing light. This is also the basis for research in the new fiber-based optofluidic sensing devices. Optofluidic devices allow small, well-controlled volumes of analytes to interact efficiently with the optical field, e.g., enabling tailored optical interrogation methods for localized sampling and analysis.

The purpose of this Msc thesis project was to develop a fiber-based optofluidic system for detecting biological samples with a limit of detection of around nano-molar or less. The system parts were carefully chosen with the experiments. Once the system was built, then the system was tested for the limit of detection (LOD) using a fluorescent dye. Afterwards, fluorescent beads were also used for simulation of a biological sample. When it passed this test, then the final experiment proof would be performed which should consist of detecting EGFP bacterias.

There are two acknowledged types of optofluidic devices; planar optofluidic devices and fiber-based optofluidic devices. Planar optofluidic devices use planar photonic structures such as integrated planar waveguides or photonic crystals to guide the light. These can be very compact but requires significant investment in design, fabrication time, and cost. The fiber-based optofluidic devices use optical fibers of various designs for guiding the light, microfluidic transport, or both. The advantage with fiber-based optofluidics is, as stated earlier, due to the well-established utilization of optical fibers and the potential to integrate microfluidic environments using commercially available components, thus minimizing the development efforts. The surface smoothness is of the order of 100 pm in optical fibers while it is 1,4 nm for typical planar optofluidic material such as silicon on

insulator.[9, 10] The smooth surfaces provide low optical loss and guarantees that the microfluidic flow will behave in a classical, theoretical behavior.

1.1 Disposition

This thesis starts with a review of some of the background in optofluidics, where, e.g., some of the fluid dynamics involved is explained. Then the setup components and their functions are described in some detail, followed by the techniques of splicing and access-hole fabrication. The data from the fluorescent dye, beads, and E-coli bacteria are presented, followed by a discussion and a conclusion.

2 Theory

Optofluidics is the combination of microfluidics with optic technology. Microfluidics is a technology that involves extremely small volume of fluids (femto- to microliters). The overall dimensions of a device can vary but the dimension of the channel cross-section, where the fluid flow, is in the micrometer range.

Microfluidics started with the inkjet printers at IBM in the late 1970s[11] and later continued with microfluidic devices developed in the early 1990s.[12] Since then, the field has advanced giving rise to the new field of optofluidics. Optofluidics has shown various applications due to the strong advancement of the photonics field, for example two-hole fibers (THF), photonic crystal waveguide[13] and quantum dots[14].

The first goal of the project was to make a simple optofluidic system, which meant the fibers, capillaries, and other equipments that had to be chosen. We decided to employ a fiber-based optofluidic system for the reasons that have been given in the introduction. The plan was to insert a sample in the system that should be detected. We wanted the emitted light from the sample to be efficiently collected meaning the fiber should be close to the same sample with a large NA. The fiber layout is shown below in Fig 2.1:

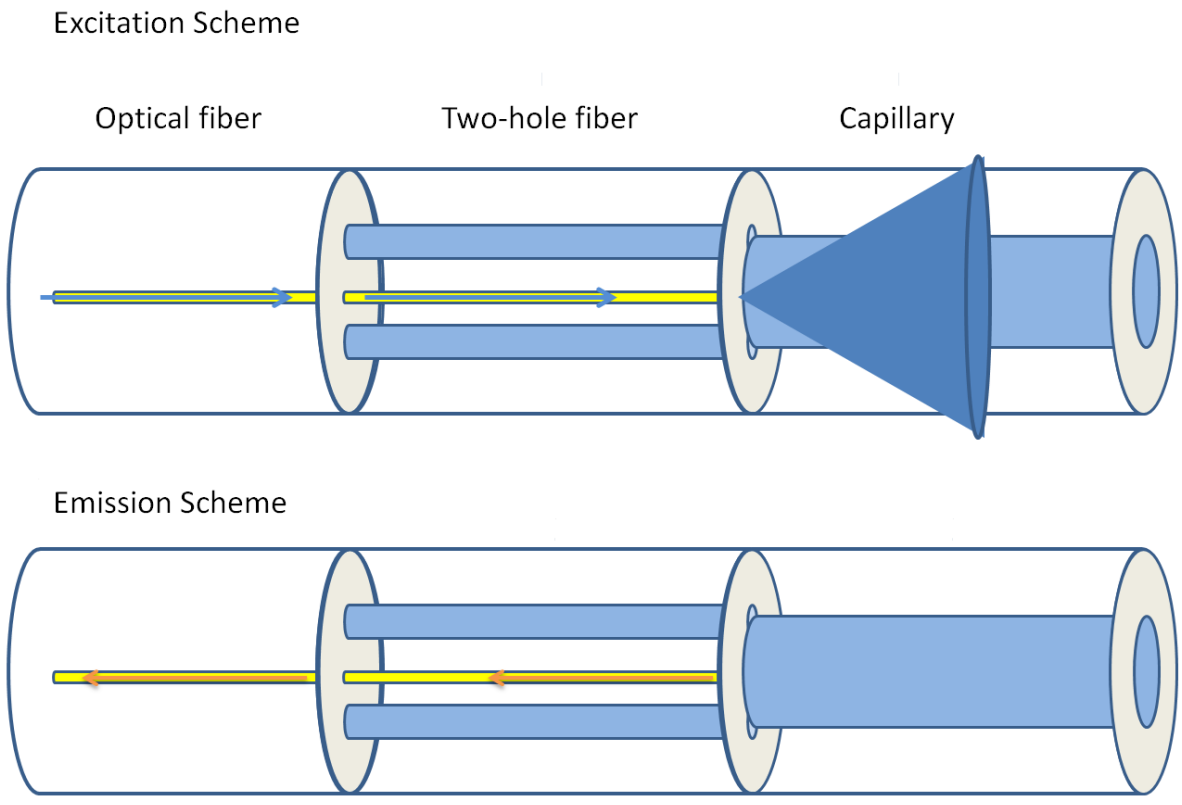

Figure 2.1: The fiber layout showing two schemes; excitation and emission scheme. The laser light is entering from the left side using an optical fiber, which is diverging out from the two-hole fiber to the capillary. The blue arrow and cone represents the blue laser (excitation wavelength). The sample will be inserted from the right side using the capillary, which can then flow into one of the two holes. The emission fluorescence, (represented by the orange arrow) will be isotropically released from the sample assuming it is in the (blue) cone of excitation light and part of the emission will enter into the core (yellow cylindrical shape in the middle) of the two-hole fiber. This will then exit out from the optical fiber for detection.

We can see that three different kinds of fibers are required for this setup; the optical fiber, the optical fiber with hollow axial part for the flow of the sample and the capillary for inserting the sample. The two-hole fiber was chosen because the sample has to flow somewhere. The two holes could also come in handy for filtering the samples of interest in a different hole. Manipulating the samples into different holes is not the scope of this thesis, though. These three fibers have to be joined together somehow, without introducing optical loss and leakage of the sample. Arc fusion is a well-known method, which fits perfectly for this purpose. This is explained thoroughly in Chapter 4.1.1 Fusion.

The fluid is flowing from the right hand side but it also has to exit somewhere to create a flow. This meant that the two-hole fiber requires an exit meaning the capillary part of the THF has to be accessed by some means, for example, by drilling in the hole. Various methods have to be investigated to find an effective and reproducible method to make holes in two-hole fibers. The different methods are described in detail in chapter 4.1.2 Formation of Access Holes.

Once the fiber layout was completed, the other components had to be selected. A blue laser (491 nm) was chosen which is well known to be used for analysis of biological samples. The Photomultiplier tube (PMT) is a well-known, sensitive detector when it comes to microfluidics and blue/UV radiation. We will need optics to guide/concentrate the beam as well as minimizing the intensity of certain wavelengths, which we are not interested in (filters). The layout is shown below in Fig 2.2:

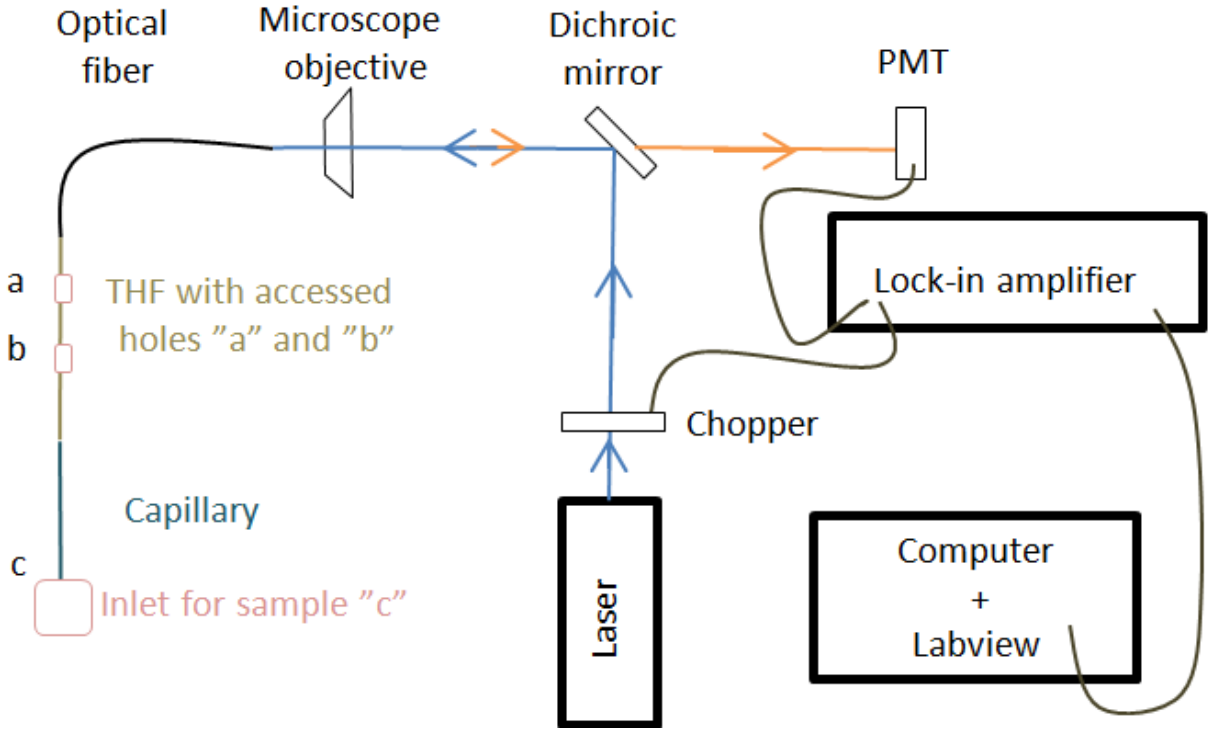

Figure 2.2: The initial layout of the setup. The dichroic mirror makes sure that blue laser (blue arrow) and emission wavelength (orange arrow) go to their respective direction. The emission originates from the interface of the THF and the capillary. The filters are placed close to the PMT. The PMT signal is sent to a lock-in amplifier where it is amplified and filtered thene it is sent to a computer and handled with labview.

The lock-in amplifier and chopper are used for getting a high signal-to-noise (SNR) ratio described in Chapter 3.1.1.6 Lock-in Amplifier , Chopper and Photon multiplier tube (PMT). We need to try out different filters to find the best signal-to-noise ratio. After this setup was completed, then three tests have to be performed to show the performance of the total system.

The three tests consist of detecting different concentrations of fluorescent dye to find the limit of detection (LOD). This test is useful for determining the performance and optimization of the setup. Once a satisfying LOD was achieved then the fluorescent beads, also known as microspheres were tested. These beads are tagged with fluorescent molecules and act as a simulation for a biological sample. This test showed its readiness for the final test, which is detecting a real bacteria (EGFP).

The objective of this MSc thesis project is summed in the table 2.1 shown below:

Objective: build a fiber based optofluidic system for detection of biological sample	
Research required in	**Reason**
Fusion	Optimal fusion parameters for fusion between different fibers for low optical loss and keeping hole integrity
Formation of access holes to THF	This is required for the flow of fluid in the system. The hole should be clean to prevent blockage
Filters	Specific filters have to be checked to get the best set hence to find optimum Signal-to-noise ratio
Detection of fluorescent dye	Detection of different concentration of fluorescent dye will provide LOD showing the setups performance
Detection of fluorescent beads	This is a simulation for biological sample in a controlled way to see if individual beads are detected
Detection of EGFP bacteria	This is to demonstrate its application and to fulfill the objective

Table 2.1: This table clearly states the objective and the means to achieve it.

It is essential to understand the basic fluid concepts because there exists important differences when the dominant physical quantities change between macro and micro scale devices. For example, in the microfluidic regime, laminar flow characterized by low Reynolds number will fully dominate. There are two well-known methods of flow propulsion, which is known as pressure driven flow, and electroosmotic flow (EOF), respectively. The pressure driven flow is a basic way of propulsion and has a higher analyte broadening due to dispersion caused by the parabolic flow profile.

Simple understanding of the fiber is also required as it is being heavily employed in the system. The fiber consists of a core and cladding with different refractive indices to guide the light. It is generally speaking difficult to achieve a good coupling from free space into the fiber since a part of the beam can even enter the cladding.

2.1 Basic Fluid Concept

The theory and equations for Chapters 2.1 and 2.2 are taken from a book called, "Encyclopedia of microfluidics and nanofluidics," by D. Li.[16] The viscosity (μ) of a fluid is a measure of the fluid's resistance to flow when an external force (originating from a pressure difference or electro-osmosis) is applied as shown in Fig 2.3.

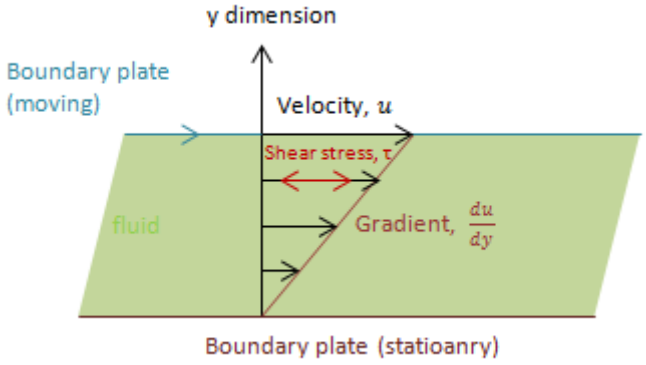

Figure 2.3: Laminar shear of fluid between two plates. The friction between the fluid and the boundaries causes the fluid to shear. This type of flow is known as Couette flow .

The equation for dynamic viscosity is:

$$\mu(Pa \cdot s) = \frac{\tau}{\frac{du}{dy}} = \frac{\frac{F}{A}}{\frac{du}{dy}} \quad , \tag{2.1.1}$$

where τ is the fluid shear stress that is given by a force (F) divided by the area of the plate (A), u is the velocity and y is the distance between the two plates. The $\frac{du}{dy}$ is the rate of strain (gradient) and the viscosity is measured in Pascal times second.

The Reynolds number (Re) is a dimensionless measure of the ratio between the inertial forces and the viscous force in the fluid.

$$Re = \frac{Dv\rho}{\mu} \quad . \tag{2.1.2}$$

Here, D is the fluid cross-sectional diameter (m), v is the velocity (m/s), ρ is the density (kg/m^3) and μ being the viscosity (Pa*s). If the Reynolds number is smaller than 1500-2000, then it is a laminar flow while if it is greater than 4000, it means turbulent flow.[15] If the Reynolds number is between 2000 and 4000, it can both be turbulent or laminar depending on the pipe roughness and flow uniformity. In laminar flow, the fluid flows without being mixed with the neighboring streamlines except through molecular diffusion while in turbulent flow, the fluid moves in such a way that the velocity and pressure varies in time.

Let us assume the liquid is water ($\mu = 10^{-3}$kg/s x m, $\rho = 10^3$ kg/m^3) in a 5 cm diameter pipe flowing at 1 m/s and with a 50 µm diameter capillary flowing at 1 mm/s (In reality, it flows lower than this). The following Reynolds number will thus be:

$$Re(Pipe) = \frac{Dv\rho}{\mu} = \frac{5 \times 10^{-2}m \times \frac{1m}{s} \times \frac{10^3 kg}{m^3}}{\frac{10^{-3}kg}{s} \cdot m} = 5 \times 10^4 >> 2000 \quad , \qquad (2.1.3)$$

$$Re(Capillary) = \frac{Dv\rho}{\mu} = \frac{50 \times 10^{-6}m \times \frac{10^{-3}m}{s} \times \frac{10^3 kg}{m^3}}{\frac{10^{-3}kg}{s} \cdot m} = 0{,}05 << 1500 \quad . \qquad (2.1.4)$$

This shows that the laminar flow is dominating in the capillary, which is also the case for our THF.

2.2 Microfluidic Dynamics

The fluid dynamics can be represented by the Navier-Stokes equations. These equations are derived by applying Newton's second law to fluid motion.[16]

$$\rho\left(\frac{\partial u}{\partial t} + \boldsymbol{u} \cdot \nabla \boldsymbol{u}\right) = -\nabla p + \mu \nabla^2 \boldsymbol{u} + \boldsymbol{f} \quad . \qquad (2.2.1)$$

Here, $\rho\left(\frac{\partial \boldsymbol{u}}{\partial t} + \boldsymbol{u} \cdot \nabla \boldsymbol{u}\right)$ represents the inertia, $\frac{\partial \boldsymbol{u}}{\partial t}$ is the acceleration, $\boldsymbol{u} \cdot \nabla \boldsymbol{u}$ is the convective acceleration, $-\nabla p$ is the pressure gradient, $\mu \nabla^2 \boldsymbol{u}$ is the viscosity and $\boldsymbol{f}$ represents the body forces (per unit volume) acting on the fluid. This equation is very important for describing the electroosmosis and pressure driven flows. I am not going to derive the equations here, but it can be gleaned from the text-book.[16]

2.2.1 Pressure Driven Flow

We will consider that steady pressure is applied and a no-slip boundary condition exists for the capillary. We also assume that the external forces such as gravitaty to be negligible which holds true for a capillary with large ΔP. The pressure force that pushes the fluid through the tube is related to the cross section area (πr_c^2) times the pressure drop (ΔP) which is balanced by the drag force exerted by the capillary wall. The viscous forces resisting the shear stress (see Figure 2.3) is associated with the area (A) of contact between the capillary wall and the fluid ($2\pi r_c L$), where L is the length of the capillary. By equating the pressure force and the viscous force, we get:[17]

$$\pi r_c^2 \Delta p = -2\pi r_c L\eta \left(\frac{du}{dr}\right)_0 \quad . \tag{2.2.1.1}$$

This equation does not just apply for the wall; it can also be applied for any arbitrary radius r within the inner cylinder. It can be written as:

$$du = \frac{-\Delta p}{2L\eta} r dr \quad . \tag{2.2.1.2}$$

After integrating Eq (2.2.1.1), we get:

$$u = \frac{-\Delta p}{4L\eta} r^2 + constant \quad . \tag{2.2.1.3}$$

Applying the condition u = 0 at the wall (where r = r_c) yields the constant$\left(\frac{\Delta p r_c^2}{4L\eta}\right)$, which results in the following expression:

$$u(r) = \frac{\Delta p}{4L\eta}(r_c^2 - r^2) \quad . \tag{2.2.1.4}$$

The parabolic velocity profile is drawn by using MathCAD, and the result is inserted in the capillary as shown below in Fig 2.4:

This shows that the flow velocity is highest in the middle while it approaches zero value on the walls. This will mean that in a real experiment, some beads might flow faster than others depending on the radial position.

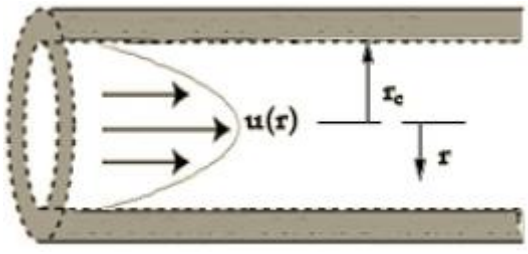

Figure 2.4: Profile of pressure driven flow in the capillary. The velocity is highest in the center while it approaches zero at the walls.

2.2.2 Electroosmotic Flow

When a voltage difference (V) is applied between two ends of a buffer-filled capillary then a plug flow can be created within the system, which is known as electroosmotic flow (EOF). [18, 19] The fused silica in a capillary or holes-fiber have silanol (Si-OH) groups attached to the interior wall which are

ionized to negatively charged silanoate (Si-O$^-$) groups for pH values greater than three. This negatively charged silanoate creates a layer of cations near the surface which will maintain the charge balance close to the wall. This forms the electrical double layer (EDL) of ions and a potential difference known as the zeta potential.

When an external voltage, V, is applied axially, the cations in the positively charged sheath (containing surplus ions) are attracted to the cathode along the entire length of the capillary. By entraining the bulk fluid, the flow profile becomes radially uniform (plug flow) which is seen in Fig 2.5. The zeta potential (ζ) is strongly dependent on the pH value because it is determined by the degree of ionization. Due to this, the flow is higher at high values of pH.[20]

The EOF (ν_{eo}) is defined by the following expression:[20]

$$\nu_{eo} = \mu_{eo} E = \frac{\in \zeta}{4\pi\eta} E \qquad . \qquad (2.2.2.1)$$

Here ∈ is the dielectric constant, μ_{eo} is the electroosmotic mobility, E is the electric field and η is the viscosity of the buffer. A main advantage of the EOF is that it is possible to sweep the whole bulk liquid in the specific order: cations, neutrals and anion considering that the pH is neutral to alkaline.

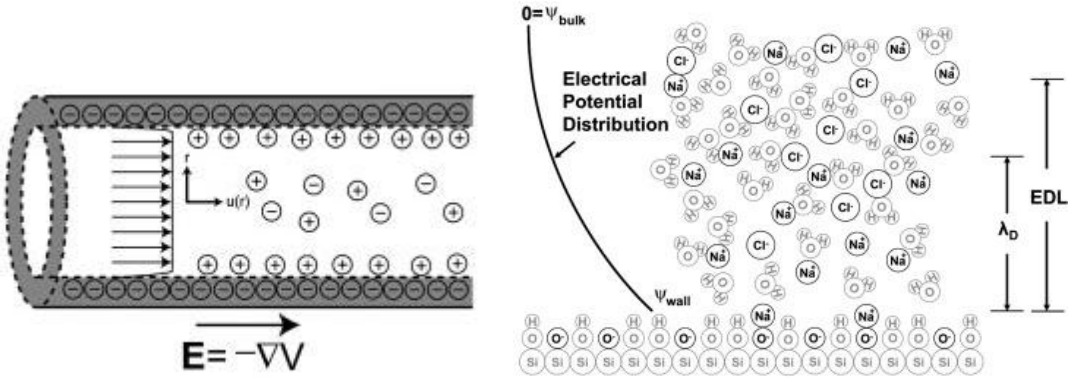

Figure 2.5: Capillary driven by EOF. The plug shape is in range of nanometers. The flow is uniform except for the walls where the velocity approaches zero. [14]

The plate count (N) is a measure of how efficiently the analyte peaks are transported by electrophoresis through a capillary, which is given by:[16]

$$N = \frac{(\mu_{ep} + \mu_{eo})V}{2D_m} \qquad . \qquad (2.2.2.2)$$

Here μ_{ep} is the electrophoretic mobility, D_m is the solute's diffusion coefficient and V is the applied voltage. This means that very high plate counts can be generated by macromolecules, which have small diffusion coefficients, by increasing the voltage.

The resolution, R, between two different species is given by:[16]

$$R = (0.177)\frac{\mu_{ep}\sqrt{V}}{\bar{\mu}_{ep}\sqrt{D_m}} \quad . \qquad (2.2.2.3)$$

Here the $\bar{\mu}_{ep}$ is the median electrophoretic mobility. This shows that increasing the voltage is a limited way of improving the resolution since doubling the resolution requires quadrupled voltage. The best way, then, to get better resolution is to obtain a good control of the mobility, which can preferably be accomplished by the selection of an appropriate buffer.

There is a voltage limit as high voltage causes Joule heating (Joule = I^2R). This is a consequence of the resistance of the buffer to the flow of current. The rate of heat generation can be approximated as:[16]

$$\frac{dH}{dt} = \frac{kV^2}{L^2} = kE^2 \quad . \qquad (2.2.2.4)$$

Here k is the conductivity, L is the capillary length, and E is the applied electric field. The equation indicates that to decrease the heat generation, the voltage has to be decreased or the length has to increase. This is the main reason why the voltage was maximum 20 kV in our setup, while the length of the capillary was around 70 cm. Another reason for the voltage to be around 20 kV was to minimize the chances of corona discharge, which otherwise might destroy the electronics. It should also be noted that a significant decrease in the electric field would reduce the efficiency and the resolution.

Temperature gradients occur due to the heat dissipation. The heat is dissipated by diffusion toward the wall meaning that the temperature is higher in the middle compared to the walls. The temperature drop as a function of radial position, r, can be written as:[16]

$$\Delta T = 0{,}24\frac{Wr^2}{4K} \quad . \qquad (2.2.2.5)$$

Here W is the power, r is the capillary radius, and K is the thermal conductivity. This equation shows that narrow-diameter capillaries are more efficient because the current passed through the capillary is reduced by a factor of r^2 and the heat is more readily dissipated across a narrower radial path. However, narrow diameters may cause increased sample adsorption. We can sum up these arguments in the Table 2.2 as shown below:

Variable	Effect
Decreasing electric field	Proportionally decreases heat generation Reduces efficiency and resolution
Reducing capillary inner diameter	Twice as much decrease in current Decreases detection sensitivity Might cause sample adsorption
Increasing capillary length	Twice as much decrease in heat generation Better separation if analytes have different charges
Decreasing buffer ionic strength or concentration	Proportionally decreases current Might cause sample adsorption

Table 2.2: Summary of the effects of different variable in the system.

2.3 Optics

The concept of total internal reflection (TIR), which is responsible for guiding the light in optical fibers, has been known at least since 1854.[21] Glass fibers were introduced in the 1920s but their first practical use was in 1950s when the cladding medium was introduced, which considerably improved the guiding.[22] Before 1970, optical fibers were mainly used for medical imaging over short distances because of high optical losses.[23] In 1970, low-loss optical fibers were introduced and further progress was made in 1979, which lead to loss reductions down to as low as 0.2 dB/km, near the minimum at 1.55 µm wavelength.[24] The manufacture improvements and the demand for different types of fibers have resulted in different specialty fibers such as THF, holey fiber, carbon fiber, dispersion-shifted fiber and more.

2.3.1 Geometrical Optics

An optical fiber consists of a cylindrical core of silica glass surrounded by a cladding[25]. The core has higher refractive index compared to the cladding, here shown for a step-index fiber, Fig 2.6.

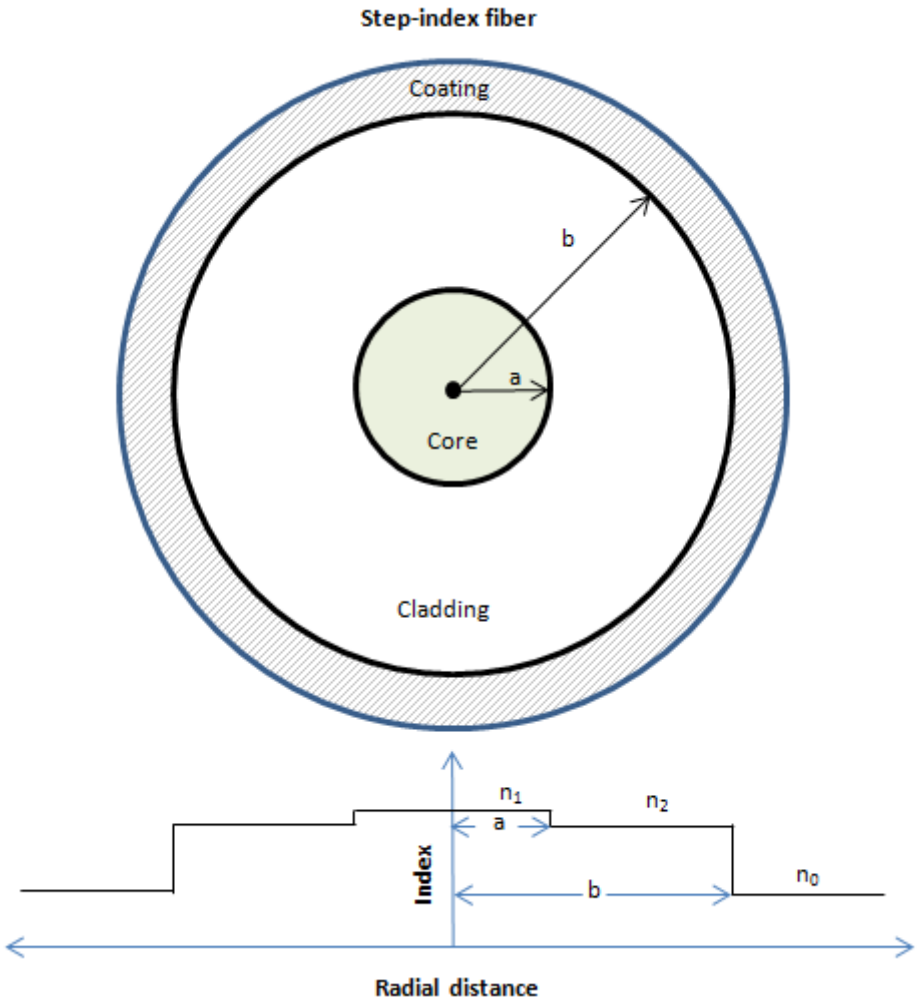

Figure 2.6: Cross section and refractive index profile for step-index fiber.

The geometrical-optics description is a simplified picture (see Fig 2.7), which can be used when the core radius, a, is much larger than the light wavelength, λ. When the light with an angle θ_i enters the core, the ray is refracted toward the normal. The angle, θ_r, of the refracted ray is given by Snell's law:

$$n_0 \sin\theta_i = n_1 \sin\theta_r \quad , \qquad (2.3.1.1)$$

where n_0 and n_1 are the refractive indices of the air and the fiber core, respectively. The refracted ray hits the core-cladding interface and is reflected if $\sin\emptyset < \frac{n_2}{n_1}$. The critical angle $\emptyset_c$ is defined by:

$$\sin\emptyset_c = \frac{n_2}{n_1} \quad , \qquad (2.3.1.2)$$

where n_2 is the cladding index. Total internal reflection (TIR) takes place throughout the fiber when all rays with $\emptyset > \emptyset_c$ is confined in the core.

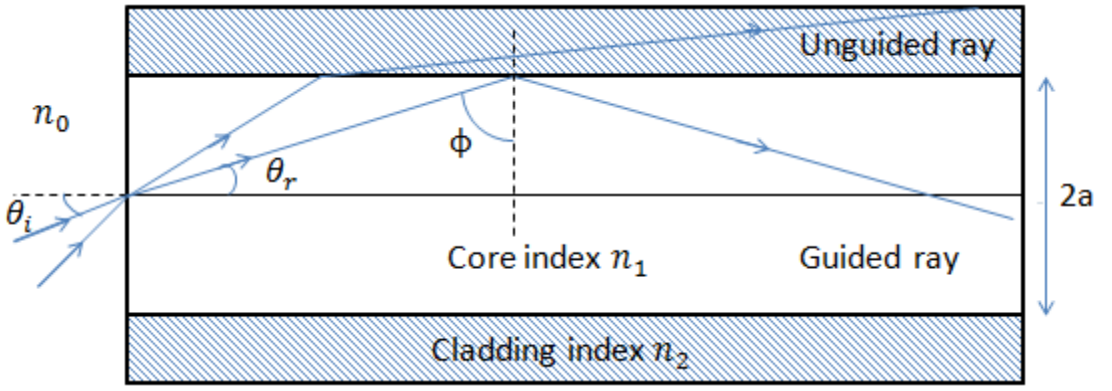

Figure 2.7: Total internal reflection (TIR) in step-index fiber. Rays where $\emptyset < \emptyset_c$ are refracted out of the core.

The numerical aperture (NA) is a dimensionless quantity that determines the range of angles of light that the fiber can accept or emit. The NA can be obtained by substituting $\theta_r = \frac{\pi}{2} - \emptyset_c$ in Eq (2.3.1.1):

$$NA = n_0 \sin\theta_i = n_1 \sin\emptyset_c = (n_1^2 - n_2^2)^{\frac{1}{2}} \quad . \qquad (2.3.1.3)$$

It is important to have a large NA in order to couple maximum amount of light into the fiber.

2.3.2 Coupling from Free Space

It is often difficult to couple in a laser beam from free space to the core of a fiber since the minimum waist of the focused beam is about the same size as of the core (2a). If not coupled in correctly, then the beam will travel in the cladding that can induce fluorescence from the acrylate coating and less power will be used for exciting the sample. The fluorescence can increase the noise in the system, which will be explained in more detailed in the Chapter 3.1.1.2 Carbon Coated Fiber. The expression for determining the minimum beam waist is given by:

$$w_0\theta_0 = \frac{\lambda}{\pi}M^2 \quad , \tag{2.3.2.1}$$

where w_o is the focused beam radius called the spotsize, θ_0 is the half-angle beam divergence, λ is the laser wavelength, and M^2 is the beam quality factor (M^2>>1). Thus, the minimum diameter is:

$$d_0 = 2w_0 = 2\frac{\lambda}{\pi}\frac{M^2}{\theta_0} = \left[\theta_0 \sim \frac{D_0}{2f}\right] = \frac{\lambda}{\pi}\frac{4fM^2}{D_0} \quad , \tag{2.3.2.2}$$

where d_0 is the focused diameter, D_0 is the input laser beam diameter, and f is the focal distance of the objective lens (see Fig 2.8). The typical data for my experiment were $\lambda = 491\ nm$, $D_0 = 700\ \mu m$, and $M^2 = 1{,}1$. The core of the fiber is 8 µm in diameter, meaning that the focused diameter has to be less than 8 µm for optimum coupling from free space, which will require a microscope objective with focal length less than 8 mm.

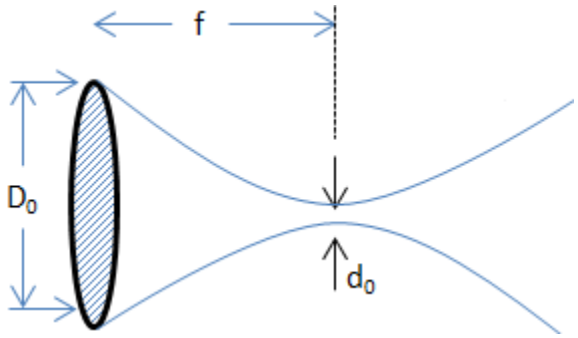

Figure 2.8: Schematic showing the variables which are used to calculate the minimum beam waist.

2.4 Conclusion

The theory for simple fiberoptics as needed for the present project has been explained thoroughly and referenced if more information is required. The experimental setup has been showed but now more detailed information of the parts of the equipment will be explained in chapter 3. We have decided so far that the shall consist of a fiber-based optofluidic system and we have explained how the fiber works. The coupling from free-space into the fiber has been explained and we will see later how difficult it is to achieve optimum coupling. There will be two types of propulsion flow in our setup; pressure driven flow and electroosmosis. The different variables for electroosmosis demonstrates the effect of the performance of the setup.

3 Apparatus Parts and their Functionality

A simple theory has been discussed in Chapter 2 and being, related to our setup so in this Chapter we will discuss the different components of our experimental apparatus with detailed specifications together with the methods used to perform these experiments.

3.1 Apparatus

The key parts of the apparatus consist of a mixture of optical and fluidic components. Integration of fluidic and detection modules, requires that the fabrication enables sensitive detection of the sample to be performed in the capillary, fused with the optical fiber. Coupling of the excitation and emission light will be efficient if the liquid sample is in close proximity to the core. The detection and fluidic parts of the apparatus will be explained in detail in the following.

3.1.1 Detection and Fluidic Components

The majority of the performed experiments concerning the detection were made in order to find the optimum SNR, here considered to be the most important figure of merit. The optical and fluidic components will be explained in detail in the following section to make it easier to understand how the entire setup works.

3.1.1.1 Two-Hole Fiber

In order to have an all-fiber system, a two-hole fiber (THF) was selected to be a central optofluidic candidate. The THF has a core diameter for guiding light that is around 8 μm while the capillary holes are 28 μm in diamter (see Figure 3.1). The THF length was around 20 cm. One advantage of having two holes or more includes the possibility of individual flow-based selection, since it should be feasible to guide certain beads or molecules to a specific hole. Another benefit is that the 28 μm diameter hole is excellent for heat dissipation (see Eq 2.2.2.5). The two holes were first accessed through individual grinding by placing them vertically aligned using glue as support (since the grinded parts easily break). Subsequently, additional support was also applied by the use of silicon glue buffer reservoirs.

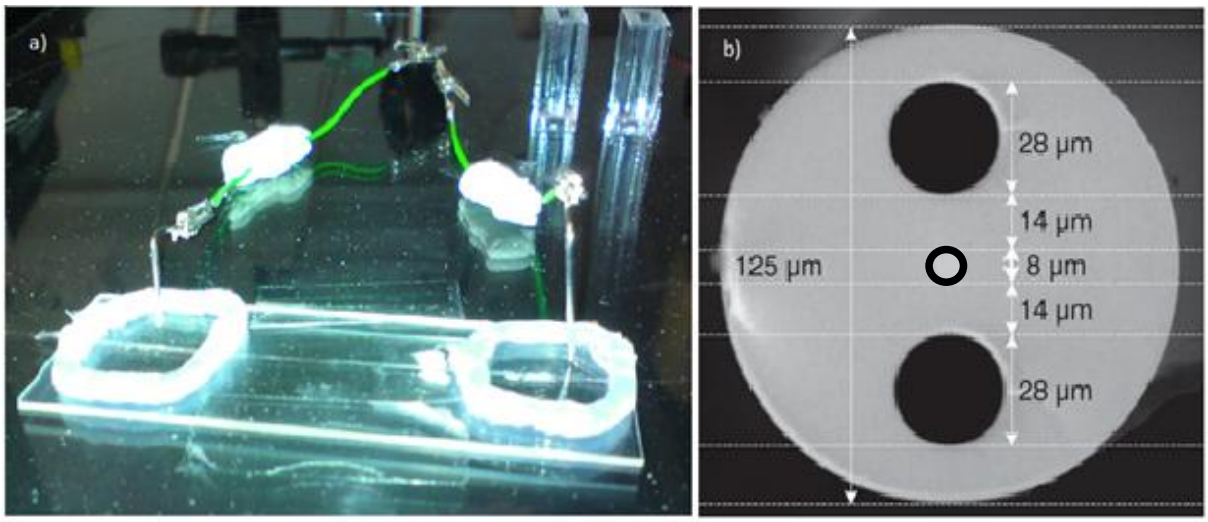

Figure 3.1: a) Photograph displaying the THF on a slide with platinum electrodes placed in silicon glue reservoirs. In each reservoir, a different hole is accessed. Look at figure 3.10 to understand it clearly. b) SEM picture showing the cross-section of the THF with specified dimensions.

3.1.1.2 Carbon Coated Fiber

Initially, an ordinary telecom single-mode fiber SMF28 (Corning) was the waveguide candidate of choice (see Fig 3.2), but when we just had the laser coupled to the SMF28 and we noticed a lot of background fluorescence being generated. We inspected the fiber using a color filter (OG515, Schott GmbH), which revealed that a lot of background fluorescence from the SMF28 fiber was being generated, apparently originated from the protecting acrylate polymer. This meant that we needed to perform another experiment in order to compare the SMF28 with a carbon-coated fiber, which is not mentioned in Table 2.1.

A small test was done to check if the acrylate coating introduced noise in the system. It was observed that, with the coating, fluorescence was generated around 515 nm wavelength and a part of it could probably enter into the PMT by reflection, thus reducing the SNR. The flame from a lighter was used to burn off the acrylate coating. Then, the detection took place and the detection level went down. This was the reason for why a test between carbon-coated fiber and SMF28 was required.

As an alternative, a carbon-coated optical fiber consisting of core, cladding, carbon coating and polymer coating was employed.[26] The advantage of using a carbon-coated fiber for detection purposes is that carbon absorbs spurious light, so if there exists any light originating from the cladding or from the polymer, it will be absorbed. This should have the potential to diminish a large amount of the background noise, which also implies that the requirements on fiber alignment are less stringent.

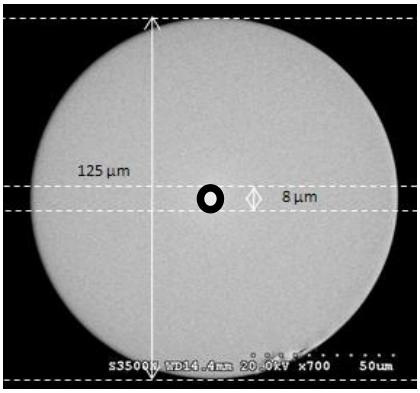

Figure 3.2: Microphotograph showing the cross section of a SMF28 with 8 µm core. The only difference with the carbon coated fiber is that there is carbon coating with thickness of 20 nm around the cladding.

Method

A comparative experiment was performed, where these two types of fiber (carbon coated and SMF 28 fiber) were dipped in 100 nM disodium fluorescein dye solution (signal), and filtered deionized water (noise) , held in a quartz container. The fiber was cleaned by Milli-Q water after dipping in the dye solution to prevent contamination of the filtered deionized water. The samples were discarded after use with each specific fiber and replenished using new samples from the same batch. The PMT voltage was set at -293 V and the power output from both fibers were 3 mW for a fair comparison with fiber lengths around 75 cm, although the PMT voltage could be set at a much higher level for the carbon fiber without saturating the signal level. The setup for this experiment is shown in Fig 3.3:

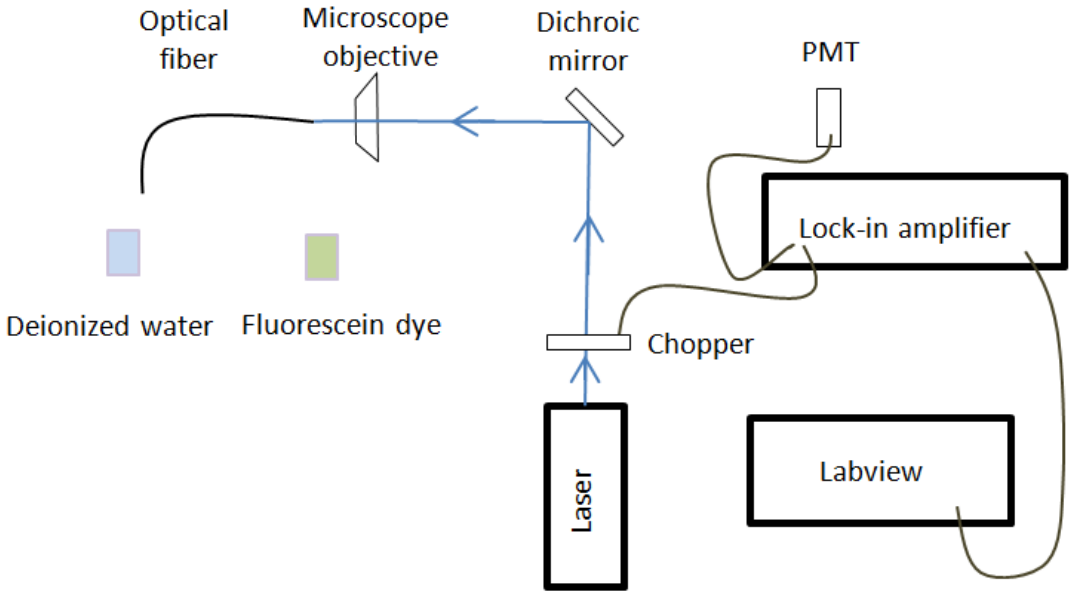

Figure 3.3: The setup where the SMF28 and carbon-coated fiber is dipped in quartz containers containing 100 nM disodium fluorescein dye solution (signal) and filtered deionized water (noise).

Result and Conclusion

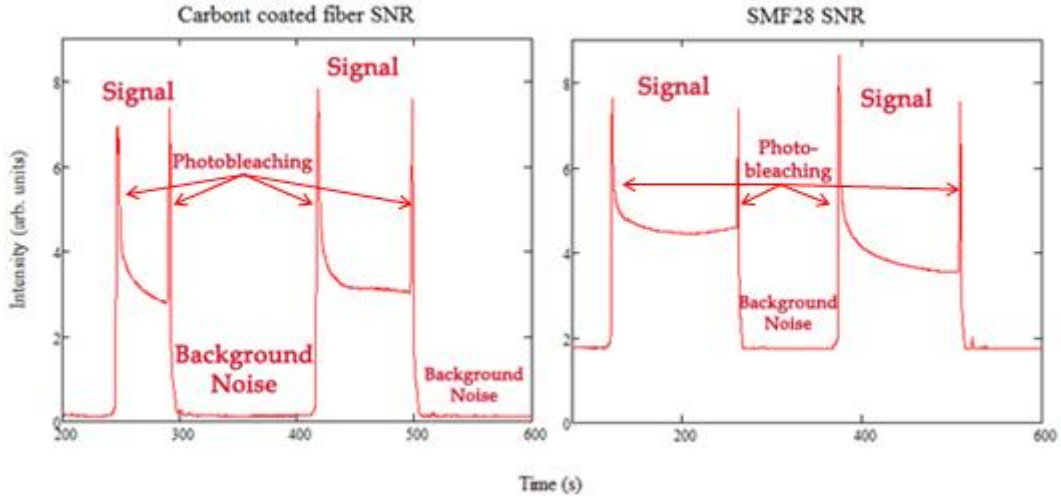

Figure 3.4: Graphs showing the signal intensity using a SMF28 and carbon coated fiber. The PMT voltage was set to -293 V and 3 mW output for both fibers cases. The disodium fluorescein dye concentration was 100 µM. It can be seen that the dye was quickly photobleached. The subsequent peak is due to the fiber being removed from the sample, as the other part of dye has not been photobleached.

It is seen from the Figure 3.4 that the noise level is much higher in the SMF28 fiber while the signal level is approximately the same. This means that one of the big contributors was the SMF28 fluorescence from the acrylate coating. The carbon-coated fiber is approximately 4 times better in terms of SNR. The detailed mean SNR together with Standard error is provided below in Table 3.1 (n = 6; the n represents the data points):

Name	Mean SNR	Standard Error
SMF28	1.1×10^3	200
Carbon coated fiber	4.2×10^3	600

Table 3.1: The mean SNR and standard error (n = 6) is given for the SMF28 and carbon coated fiber. This result encourages the use of carbon coated fiber for optimum SNR.

3.1.1.3 Capillary

The capillary we used had a 56 µm inner diameter and a length of 30 cm (see Fig 3.5). The small radial dimension of the capillary allows for good heat dissipation (see Eq 2.2.2.5). One end of the capillary was fused to the THF and the other was attached to the inlet chamber.

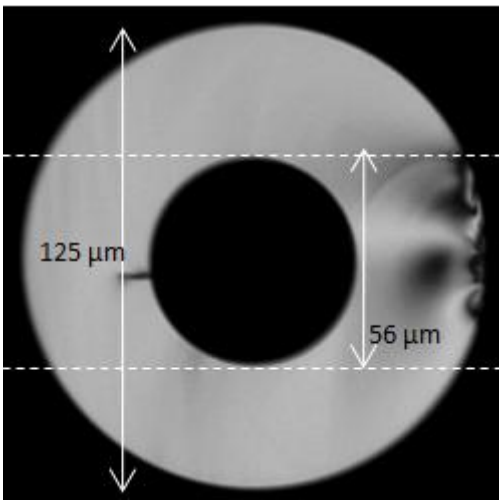

Figure 3.5: Microphotograph showing the cross section of a 56 µm inner diameter capillary.

3.1.1.4 Filters

Filters are required to enable us to attenuate the excitation signal as well as reducing unwanted signals (noise) that can come from the surroundings. The problem with most filters is that there is no filter that completely rejects certain wavelength. A small percentage of the signal will go through hence certain combinations of filters were tried out in order to find the best SNR. Each filter transmission graph was recorded using a UV-VIS spectrophotometer (Cary 50, Varian); from these various filters, data was multiplied by each other in order to theoretically calculate the best SNR. The transmission graphs can be found under Chapter appendix.

Method

Subsequently, three different filter setups were examined experimentally and the best SNR filter combination setup was chosen. The experiment was similar to that shown in Fig 3.3 (including the fiber length and power output) except that the PMT voltage was different for each filter set in order to get optimum signal. The fluorescent dye and buffer liquid was inserted in the setup as shown in Fig 2.2 using pressure-driven flow and the filters were placed in between the dichroic mirror and the PMT. The solution was moving in the fiber hence creating no photobleach effect.

The results of the various filter combinations are shown on the next page (see Fig 3.6 and Table 3.2).

Results and Conclusion

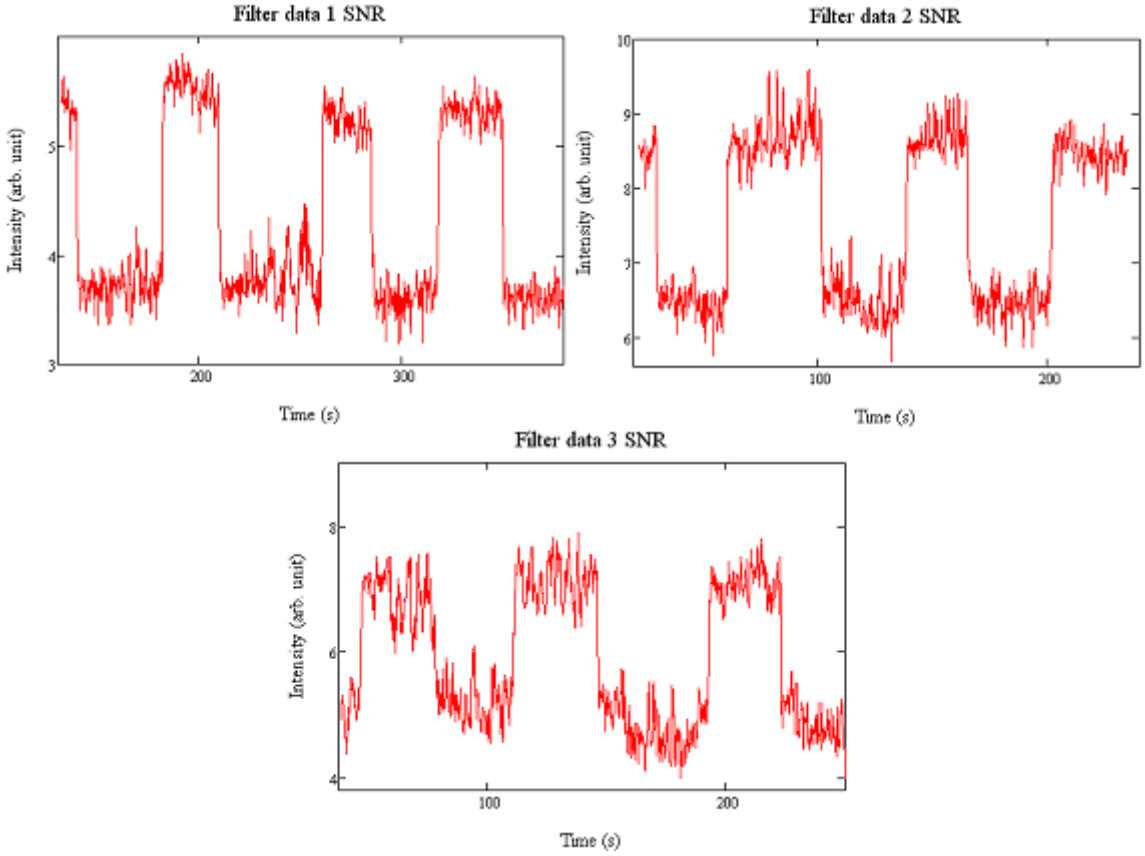

Figure 3.6: Graphs showing the SNR obtained by using different filter combinations. Each filter in different filter data is given below in the table. The filter data 1, 2 and 3 was using PMT voltage -401 V, -491 V and -476 V. The filter data 1 could use more voltage but it was calculated that the filter data 1 has better SNR hence another experiment with higher voltage was not required. This experiment was done in the fiber unlike figure 3.3.

The SNR of the three filter data set together with the standard error is given in the Table 3.2 below (n = 3):

Name	Mean SNR	Standard error
Filter data set #1 (2 of 530DF30)	16	1,4
Filter data set #2 (2 of 530DF30 and 530BP)	13	0,9
Filter data set #3 (2 of 530DF30, 530BP, and one round green filter)	10	1,1

Table 3.2: The mean SNR and standard error of different filter combinations can be seen.

This shows that the filter data set #1, which consist of two 530DF30, gives highest SNR, which is 16 ± 1,4. These filters were thus placed in front of the PMT.

3.1.1.5 Laser, Beads, and Fluorescent dyes

A continuous-wave, diode-pumped solid-state laser (Calypso, Cobolt AB) with a wavelength of 491 nm was used for the excitation. This wavelength is typical for fluorescein-based, bio-analytical applications. The output power was measured to be 25 mW and the beam quality (see Fig 2.8) for Gaussian mode was less than 1.1.

The fluorescent dye (disodium salt form of fluorescein) excitation peak was at a wavelength of 494 nm and the emission peak was at 518 nm. The dye was diluted to different concentrations: 1 nM, 10 nM, 100 nM in a 50 mM borate buffer (pH 9) to facilitate the experimental measurements of the limit of detection. During the tests, the fluorescent dye was introduced for one minute followed by a buffer. The dye represents the signal while the buffer will provide the background noise (Fig 3.7 shows the various spectral components).

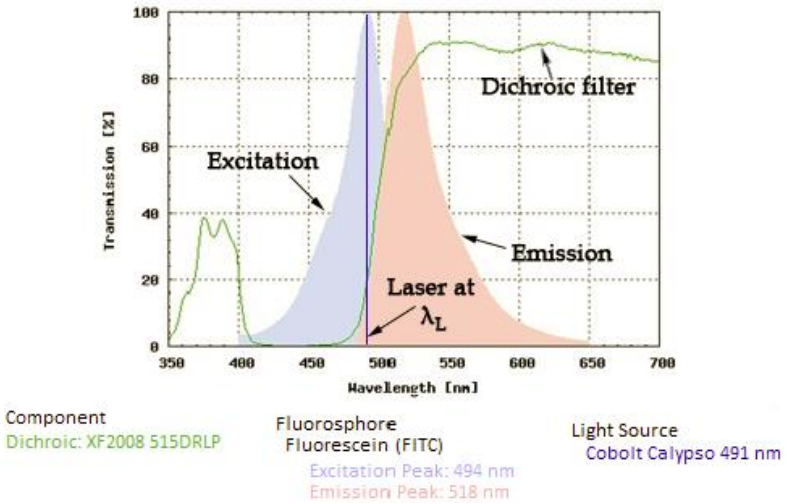

Figure 3.7: Graph showing the transmission data from the employed dichroic mirror (green curve) and the absorption and emission curves for fluorescein where violet presents the absorption wavelengths and light maroon presents the emission wavelengths. The laser wavelength is shown in dark blue color. It is seen that dichroic lets through almost 19% of the laser wavelength hence additional filters were required at the PMT. This FITC transmission graph is similar to the one, which will be used in the experiments for finding optimum filter set, carbon coated fiber and SMF28 comparison. [27]

The size of the fluorescent beads (fluorospheres sulfate microspheres, yellow-green fluorescent (505/515) *2% solids, Invitrogen) are around 4 µm and are used in order to obtain an analytical figure of merit. Thereby we could mimic a real-live cell application. The reason for this is uniformity, photochemical and physical stability caused by the constant size and fluorescent dye concentration that is contained in each of the beads.[31] The fluorescent beads were serially diluted with borate buffer for the experiment in order to avoid detection of aggregates of bead. The transmission data is presented below (see Fig 3.8) for the fluorescent beads.

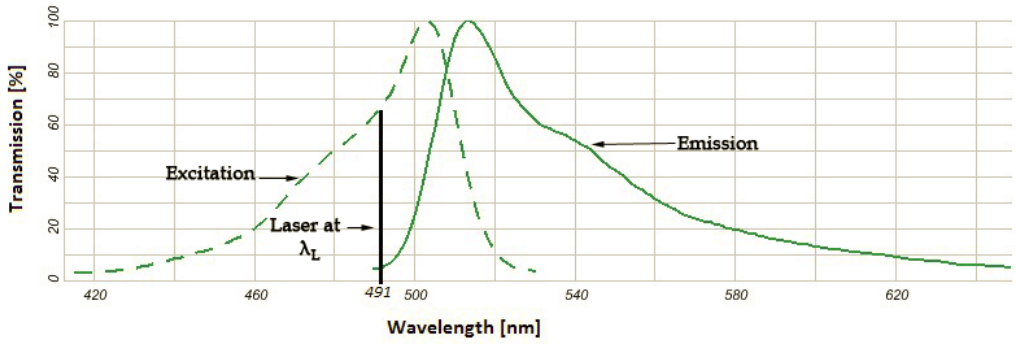

Figure 3.8: Graph showing the transmission data of fluorescent beads. The excitation peak is at 515 nm (dotted line) and emission peak is at 530 nm (line). The excitation wavelength from the laser is 491 nm (black line) meaning the excitation efficiency is around 65 %. The transmission wavelength (530 nm) will be efficiently transmitted from the dichroic mirror. The data has been provided by Invitrogen.

3.1.1.6 Lock-in Amplifier , Chopper, and Photomultiplier Tube (PMT)

The lock-in amplifier uses a chopper to create a carrier wave, which efficiently can reject all frequencies except that of the carrier wave. It acts as a narrow-band frequency filter as shown in Figure 3.9. This minimizes the noise from the surroundings resulting in a much higher SNR. The analyte signal is measured using a photomultiplier tube (PMT) that is connected to the lock-in amplifier. This technique is known to increase the SNR by more than 100 times.[28]

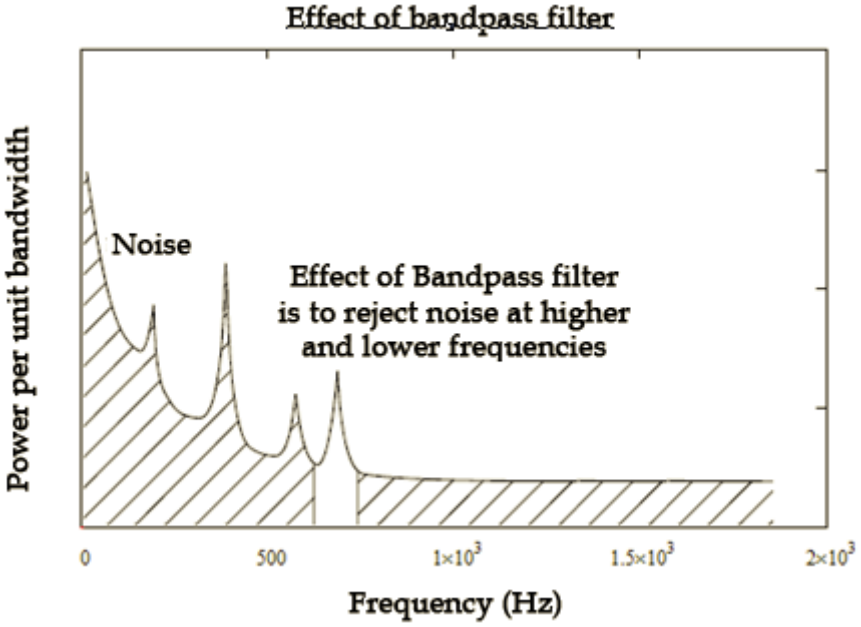

Figure 3.9: Graph showing how the lock-in amplifier acts as bandpass filter at 700 Hz, which reject noise at higher and lower frequencies.[30]

The PMT (R1463, Hamamatsu) has a very high sensitivity implying that special care has to be taken which involves keeping the room as dark as possible. One photon creates a cascade of electrons due to multiple dynode stages producing a current, which is 100 million times higher than the initial current (160 dB). This means that the spurious excitation power entering the PMT should be minimized as much as possible, hence different filters were tried to get the optimum result as discussed earlier. The signal from the lock-in amplifier was sent to the Labview for further data analysis.

3.1.1.7 High Voltage Power Supply

A high-voltage power supply (Ultravolt) was connected to a data acquisition board under Labview control, in order to manage the output voltage. The maximum voltage it supported was 20 kV. In order to be careful with corona discharges, a maximum of 15 kV was mainly used. The cathode (-) and anode (+) electrodes were made of platinum because platinum has the good characteristics of being non-reactive with the sample. There were two cathodes individually connected to the two THF reservoirs and a single anode to the inlet.

3.1.2 Fluidics

As discussed previously, there are two different ways for liquid propulsion where one is driven by electroosmosis while the other is driven by pressure (see Fig 3.10).

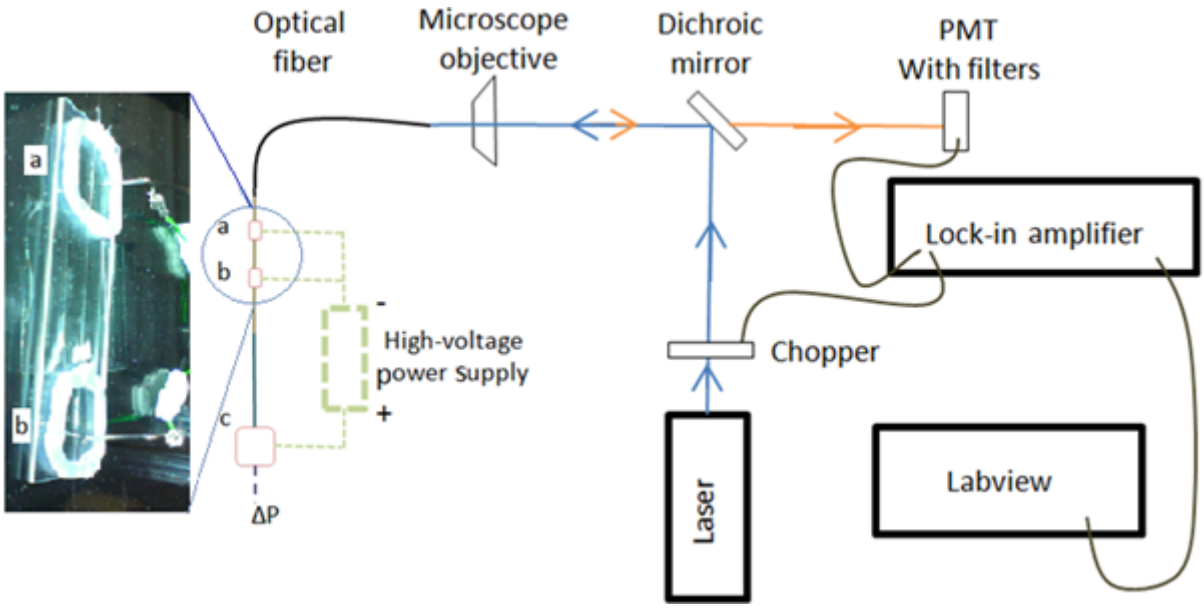

Figure 3.10: Schematic showing the setup where electroosmotic, pressure or both can control the flow. "c" represents the container which holds the sample, "a" and "b" are the reservoirs filled with buffer.

The sample is injected as a small plug from the sample container, which is represented by "c" in the figure. The reservoir "a" and "b" are filled with the buffer, completing the electrical circuit, allowing for the electroosmosis to occur. The electroosmosis commence once the HV is turned on and the sample starts to flow in the capillary. It takes around 20 minutes for the sample to reach the interface of the THF. The excitation light from the laser interacts with the fluorescent dye resulting in fluorescent emission, which is radiated isotropically. As indicated in Figure 3.10, the sample may be directed between two different flow paths terminating in either of the two reservoirs "a" and "b". The sample was injected for around 30 seconds followed with the buffer. The only difference with the setup used for pressure-driven analysis is that there is no HV power supply connected but, instead, "c" act as a pressure chamber. The junction of capillary and THF is shown in Figure 3.11.

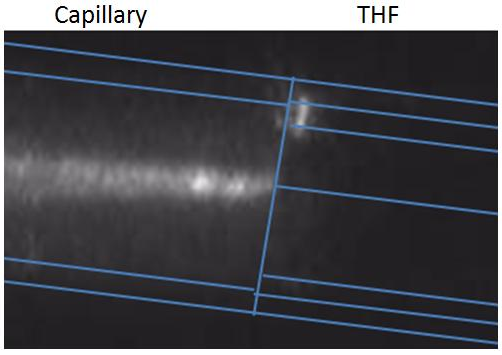

Figure 3.11: Photograph showing the laser excitation light diverging from the THF into the capillary. It is diverging out because capillary has no waveguide capability.

3.1.3 Detection

The laser excitation light (λ_L) is modulated by the chopper and is coupled to the carbon-coated fiber by a standard microscope objective (Melles Griot, 10X magnification) via the dichroic mirror (see Figure 3.1.2.1). Part of the excitation beam might leak into the cladding but will eventually be absorbed by the carbon. The beam will then travel to the THF-capillary interface and at this point diverge out from the THF through the capillary, since it has no waveguiding capability. This beam will excite the sample causing the sample to emit fluorescence isotropically at longer wavelengths ($\lambda > \lambda_L$). Part of it will be collected by the THF. The fluorescence emission will then travel via the THF and the carbon-coated fiber to the microscope objective making the beam collimated. The beam will be transmitted through the dichroic mirror, which only allows the fluorescence light, while the excitation beam or light at shorter wavelengths will be reflected (see Figure 3.7 for the transmission of the dichroic mirror). Finally, the fluorescence emission beam will pass through the emission filters and will eventually be detected as a signal by the PMT.

3.1.3.1 Minimum Detection of the PMT

To optimize the detection sensitivity, we had to make certain that the laser signal at 491 nm wavelength would be sufficiently and efficiently rejected, hence some theoretical calculations were initially performed. The minimum detectable signal for a PMT is dependent on the dark current-shot noise, because even though there is no radiation falling on the PMT, thermionic emission produces dark current noise in the PMT.

The responsitivity, R_λ, is defined as the output current divided by optical power that falls on the cathode, which gives:[29]

$$W_{min}(Watts) = \frac{(2 i_T e \Delta f)^{0.5}}{R_\lambda} \quad , \qquad (3.1.3.1.1)$$

where i_T is the thermionic emission current, e is the charge of an electron, and Δf is the signal bandwidth, which is provided by the lock-in amplifier depending on the integration time constant. The responsitivity is calculated as well by:[29]

$$R_\lambda = \frac{\eta e \lambda}{hc} \quad , \qquad (3.1.3.1.2)$$

where η is the quantum efficiency, λ is the wavelength, h is the Planck's constant and c is the speed of light. The quantum efficiency is given in Figure 3.12, showing that the sensitivity is lower for our detectable signal while higher for the laser wavelength. The rest of the information is stated in the PMT specifications provided by Hamamatsu.

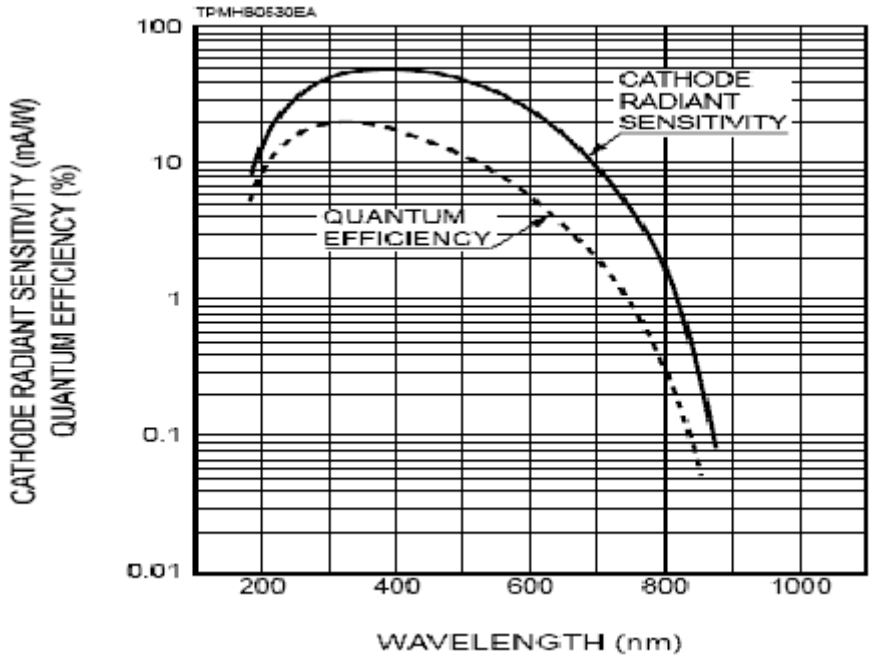

Figure 3.12: Quantum efficiency and Cathode Radiant sensitivity for the PMT.[30]

The minimum detectable signal for 491 nm radiation is calculated to be 19 pW while that for 530 nm is 26 pW. In order to see if the 491 nm optical power was sufficiently low on the PMT, the optical power was measured following the different filters by a power meter (Fieldmaster, Coherent). This investigation showed that the 491 nm optical power was only 1.6 pW, much lower than the minimum detectable signal. The measurements were performed right after the laser and the filters denoting that the actual optical power originating from the excitation wavelength on the PMT is much lower, since it additionally has to pass via the dichroic mirror. This concludes that the 491 nm radiation from the laser will not be detected by the PMT, just as we wished for.

3.1.3.2 Fluorescence Emission

The power of the fluorescence emission F is: [16]

$$F = \emptyset_f K''(P_0 - P) = K'(P_0 - P) \quad , \quad (3.1.3.2.1)$$

where P_0 is the power of the beam incident on the solution, P is the power after traversing a length b in the medium, $\emptyset_f$ is the quantum efficiency of the fluorescence process, and K" is a constant dependent on geometry and other factors. The quantum efficiency of the fluorescence is a constant for a certain system hence the $\emptyset_f K''$ can be regarded as another constant, K'. The Beer's law for liquids was used to obtain the concentration c of the fluorescent species:

$$\frac{P}{P_0} = 10^{-\varepsilon bc} \quad , \quad (3.1.3.2.2)$$

where ε is the molar absorptivity of the fluorescing molecules, b is the path length, c is the concentration and εbc is known as the absorbance, A. The equation (Beers law) can be inserted into Eq (3.1.3.2.1) which gives:

$$F = K'P_0\left(1 - 10^{-\varepsilon bc}\right) \quad . \quad (3.1.3.2.3)$$

The exponential term in Eq (3.1.3.2.3) can be expanded as a Maclaurin series resulting in the expression:

$$F = P_0 K' \left[2{,}303\varepsilon bc - \frac{(2{,}303\varepsilon bc)^2}{2!} + \frac{(2{,}303\varepsilon bc)^3}{3!} + \cdots\right] \quad . \qquad (3.1.3.2.4)$$

Assuming that the term εbc(A) <0,05, the subsequent terms in the brackets can be neglected. If all the extra terms are dropped, except for the first one, then the maximum relative error turns out to be 0,13 %.

$$F = 2{,}303 K' P_0 \varepsilon bc \quad . \qquad (3.1.3.2.5)$$

This means that the fluorescence radiant power from a solution is approximately linearly dependent on the concentration. This holds fairly true at low concentrations but, if, c, becomes so great that the absorbance, A, is larger than 0,05, the higher-order terms in Eq (3.1.3.2.4) will gradually become important, therefore losing the linearity. The practical value of the absorbance is very low in our system as the path length, b, and concentration, c, are very low, meaning that a high-power incident excitation beam is needed, hence requiring a laser.

The sample, for example a fluorescent bead, will radiate isotropically, hence regions closer to the core and within the NA will give a higher signal. There are two scenarios presented below (see Fig 3.13) and to illustrate the importance of the sample position. Scenario 1 displays one of the efficient coupling scheme, where the bead is at some distance from the core. The most efficient coupling will then be at a minimum distance from the core. Even if the sample was in the NA (dark blue triangulated shaped region) but close to the capillary wall, it will not be as efficient in the coupling as in the Scenario 1. In Scenario 2, it will not emit anything, as it is entirely outside of NA, hence no excitation takes place. This concludes that the closer the sample is to the core of the THF, the higher the signal will be.

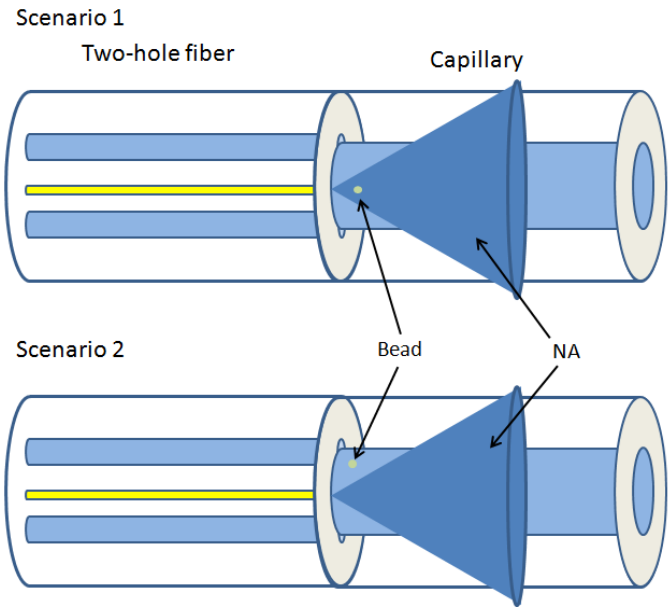

Figure 3.13: The sample (bead) positioning makes an effect on the signal intensity. Scenario 1 will give higher signal than beads, which are farther away from the core. Scenario 2 will not give any signal as it is outside of NA.

3.2 Data Analysis

In this experiment, the limit of detection (LOD) and the signal-to-noise ratio (SNR) were calculated in order to determine the performance of the setup. The SNR is defined as the ratio of the signal to the noise power. The LOD is similarly defined as the lowest amount of substance that can be detected compared to a blank (dummy) sample (containing only the background signal). The LOD is conventionally given by the amount of analyte sample or the concentration where the SNR for a certain sample is three times the standard deviation of the blank signal in order to be detected, meaning that:

$$LOD = \frac{Concentration\ (c)}{SNR - 3};\ SNR > 3 \quad . \tag{3.2.1}$$

The LOD was calculated for different concentrations to produce the estimated LOD for our setup using linear regression.

In instrumental measurements, there are usually two main types of noise, i.e., random noise and environment noise. The random noise is usually constant and independent of the analytical signal. SNR determines the main figure of merit of the system and is given by:

$$SNR = \frac{mean(Signal)}{stdev(Noise)} \quad . \tag{3.2.2}$$

The environmental noise was greatly diminished by introducing the carbon fiber, dark room environment, lock-in amplifier and using an effective emission filter in direct proximity to the PMT.

Now, the setup and the importance of the different parts should be well understood. It seems at this point that the Table 2.1 has to be modified as it was noticed that the fiber, SMF28, seemed to create a lot of fluorescent noise. The experimental setup and the details have already been described in details, so the Table 3.3 will only show the experiments which were subsequently performed:

Objective: build a fiber based optofluidic system for detection of biological sample	
Experiments	**Reason**
Fusion	Optimal fusion parameters for fusion between different fibers for low optical loss and keeping hole integrity.
Formation of access holes to THF	This is required for the flow of fluid in the system. The hole should be clean to prevent blockage.
Filters	Specific filters have to be checked to find the best set to find optimum Signal-to-noise ratio.
Selection of fiber optical cable	SMF28 introduced a lot of fluorescent background hence a better fiber was required. Carbon coated fiber is another candidate.
Detection of fluorescent dye	Detection of different concentration of fluorescent dye will provide LOD showing its performance.
Detection of fluorescent beads	This is a simulation for biological sample in a controlled way to see if individual beads are detected.
Detection of EGFP bacteria	This is to demonstrate its application and to fulfill the objective.

Table 3.3: The table showing the experiments which were done.

4 Fabrication and Detection

In the present chapter, we will examine the importance of the selection of fusion parameters, the fabrication methods, and the analyte flow propulsion in order to satisfy the needs of the microfluidics (band broadening, clogging etc.) and the optical interfaces (detection sensitivity).

The fusion parameters would determine the integrity of the hole and the waveguide. It is of utmost importance that the holes and waveguide do not deform in the process, which can lead to clogging and optical loss, respectively. The fabrication plays a vital role because the hole has to be formed in a clean manner as the debris may clog the system. The reason why we emphasized the use of a clean system is that once the capillaries gets clogged up then most likely a new system has to be assembled as unclogging is a most challenging operation. This is the reason why special care was taken in order to avoid exposing the system to dirt, debris, or air bubbles. The fluid was filtered using a 0,22 μm membrane filter to prevent dust particles, and the hole accessed THF was cleaned by ultrasound to remove as much debris as possible. The inlet chamber where the sample was placed was depressurized and checked if there were any air bubbles in the sample. The beads were treated with ultrasonic technique as well to minimize the chance of beads agglomeration since this could clog the system and give spurious high intensity peaks (we are interested only in detecting individual beads).

Once the setup was optimized, then the analysis was performed starting with a fluorescent dye to examine if the setup worked correctly and to calculate the LOD. Then the setup was examined using fluorescent beads (fluorospheres, Invitrogen) to obtain an analytical figure of merit. Thereby we could mimic a real live cell application. The reason for this is uniformity, photochemical and physical stability caused by the constant size and fluorescent dye concentration that is contained in each bead.[31] Once it passed the test, a live cell application was performed using electroosmosis to show the benefit of the system.

4.1 Fabrication

The present fabrication methods for accessing micron-sized holes in fused silica capillaries rely on very complicated and expensive equipment[32] hence alternative fabrication methods were examined to achieve clean geometrical shapes of high definition.

4.1.1 Fusion

A fusion splicer unit[33] (FSU 850, Ericsson**)** was employed to connect the different fibers and capillaries together. This procedure uses an arc discharge to melt the fibers together in a highly controlled manner. Higher reliability and lower losses can be obtained in comparison to optical fiber connectors or mechanical splices. Different fibers require different settings for optimal fusion to occur so, consequently, different settings were investigated in order to determine the best numbers for these fibers and capillaries. It was ultimately possible to use the same settings for fusing and splicing the THF to the carbon fiber and the capillary to the THF.

4.1.1.1 Method

After obtaining the specific fiber or capillary, around 5 cm of acrylate coating was removed by an adjustable stripping tool (AFS900, Thorlabs). Isopropanol was then used to clean the stripped part of the fiber. A high precision fiber cleaver (XL411, Thorlabs) was employed to cleave the fibers. Microscope inspection was used to determine the outcome of each individual cut.

It was observed to be essential that the applied discharge beam was equal on both of the optical fibers. Therefore, a central position was required for the abutted fibers. An arc discharge was generated for a determined time interval in order to allow the distal ends of the two fibers to be locally melted. Excessive amount of heat could easily collapse the air-filled capillaries or deform the core as well, which had to be avoided.[34]

Under optimal conditions, the hole integrity was preserved signified by a local surface attachment of the fiber surfaces. In order to check the fusion strength, the fusion splicer gap function was employed. The gap-function tries to create a gap between two fibers using a certain amount of force. If the integrity was maintained when the “gap”-function key was pressed, then the fusion was considered strong enough. Subsequently, the assembly was carefully placed on a microscope slide and glued to make it more robust. The integrity of the hole as well as the waveguide was important to prevent clogging and optical loss, respectively.

4.1.1.2 Result and Conclusion

It was important to choose the right parameter values for the arc fusion in order to achieve proper bonding. If incorrect values were applied, abnormalities could occur. For example, the fiber might not be axially uniform anymore, i.e., the ratio of the core to the cladding might differ at some points or the capillary diameter could even shrink so much that it could collapse, making the system inoperable (see Figure 4.1).

Figure 4.1: Micrographs showing: A) fusion done more than five times to THF and capillary junction, B) the fused capillary to THF with incorrect parameters, and C) an optimally fused THF to capillary assembly.

The optimum parameters were found to be (see Table 4.1):

Variable	Number
Prefuse time	0,3 s
Prefuse current	13 mA
Gap	40 μm
Overlap	10 μm
Fusion time 1	0,3 s
Fusion current 1	10 mA
Fusion time 2	0,8 s
Fusion current 2	10 mA
Fusion time 3	0,5 s
Fusion current 3	10 mA

Table 4.1: The optimum parameters for fusion using the THFs, the capillaries, and the carbon-coated fiber using a fusion splicer unit (FSU 850, Ericsson).

4.1.2 Formation of Access Holes

Various approaches have been investigated in order to fabricate access holes in the THF. THFs have not been earlier utilized in bio-applications mainly because there is no satisfactory way to access the individual holes. There are, however, some methods employed in microfluidic setups where the hole sizes vary from 300 µm to 1 mm[35] such as wet etching, laser micro-drilling,[36] ultrasonic abrasion, powder blasting, laser etching[37] etc. In order to be compatible with the size of the common THF capillaries, e.g., not introducing detrimental band broadening, the access holes has to be around 15 to 25 µm in diameter which requires alternative fabrication methods to be investigated. The goal was to achieve debris-free and smooth geometrical shapes.

4.1.2.1 Grinding

The use of our grinding equipment is a simple, cheap experimental method that can be bought from any hardware shop.

Method

THFs were placed on a microscope slide and glued onto several spots on the fiber for support, since the grinder can flip the fiber very easily or simply destroy it. The grinder was attached to an arm in order to carefully move it up and down in a controlled manner. The grinding process took place under a microscope. The grinder was moved up and down slowly and softly in order not to put excessive force on the fiber, which otherwise would just break. This technique required a lot of concentration and experience.

Result and Conclusion

The problem with the grinding was that much debris remained after the process and the obtained holes were very "edgy" (see Fig 4.2). A new setup were often required since the debris usually could not be unclogged. This was the main reason why careful measures were taken such as the use of filtered clean water and making sure that no dirt or air bubbles were introduced in the system that could potentially destroy the system. In order to clean the holes, air was injected into the fiber but there was still some debris left (even after a subsequent ultrasonic cleaning procedure). Furthermore, the process was not very reproducible and required an experienced user in order not to break the capillary.

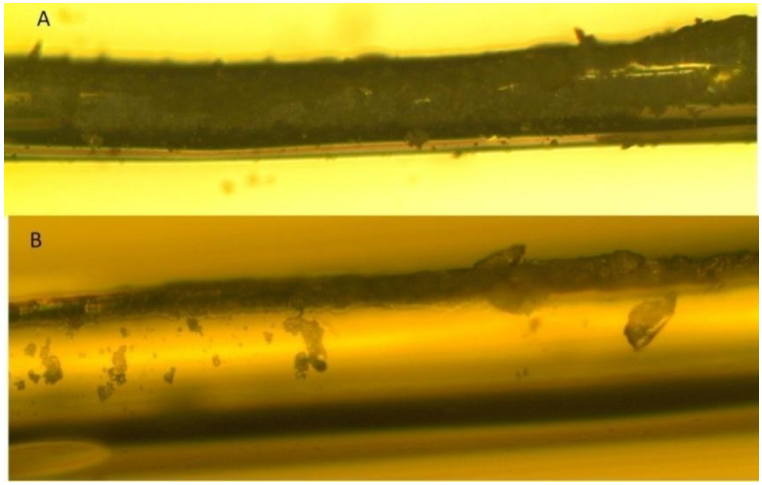

Figure 4.2: Microphotographs showing A) the grinded THF and B) the grinded THF after the ultrasonic cleaning.

4.1.2.2 Diamond-blade Sawing

This method was pursued because it has a higher lateral precision and should have the potential in generating less debris compared to grinding.

Method

The fiber was glued onto a plate and the middle portion was used for grinding. The plate was later attached to the diamond saw (normally used in our lab for sawing nonlinear crystals) slowly cutting the fiber perpendicularly to the fiber axis, at a controlled rate.

Result and Conclusion

The diamond saw has a high precision blade as it was also used to cut nonlinear crystals. The diamond-blade saw made a particular noise indicating when the capillary hole was reached. This technique generated less debris than grinding (see Fig 4.3), but, unfortunately, with the current setup, it was very difficult to attain the precision required. Thus, in order to be a functional process, the system has to be modified, i.e., employing a high precision-screw in order to obtain a better positional control.

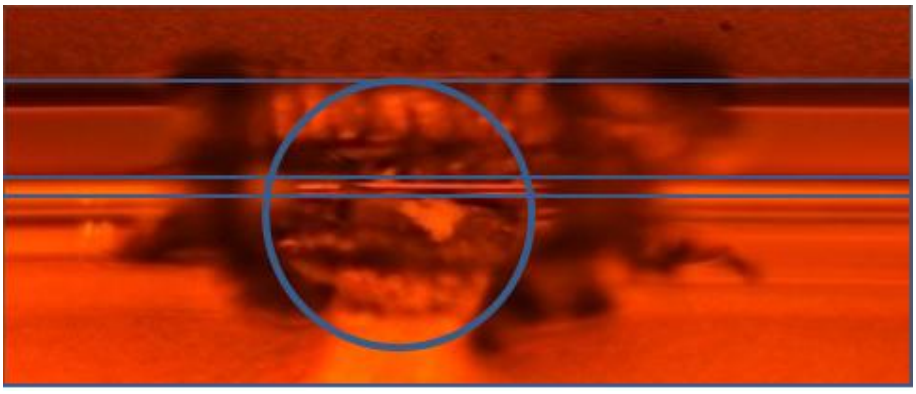

Figure 4.3: Microphotograph showing a hole created by diamond-blade saw. It produced less debris than grinding. The circle part represents the hole.

4.1.2.3 HF Etching

Hydrofluoric acid (HF) etching is a well-known wet-etching process, which is used in many different fields of technology[38].

Method

Small concentrated HF (37 wt %) drops were placed on the outside fiber surface in order to make a hole. When the hole was accessible, it should be thoroughly flushed with water to remove all the HF. In this context, it should be noted that extreme care has to be taken to properly handle HF, as it is very reactive and can be very dangerous if it drops on the human skin.

Result and Conclusion

In comparison to the mechanical means of fabricating micron-sized holes, the HF etching process could provide clean, smooth holes but required additional cleaning by flushing out the HF to stop the etching. The results in our case were unsuccessful because the acrylate coating of the fiber was not acting as a good mask. The HF liquid was spreading underneath the acrylate instead of concentrating on the selected spot. Thus, a more adhering mask that could withstand the HF treatment was required.[39]

4.1.2.4 Tesla Spark Coil Ablation

Tesla coils have traditionally been used in the past in order to check vacuum systems for leaks. If there are any leaks in the vacuum system, this can be identified by the presence of a spark. In our case, initial tests started with putting a metal wire under a thin-cover glass to see if the Tesla spark coil could be employed to make a useful hole. After a short while, a hole was formed in the glass indicating that we could use the technique for the fabrication of the access holes.

Method

Subsequently, a 20 μm gold wire was manually inserted into one of the THF capillaries under microscope inspection. The wire had to be inserted at the length of around 3 cm to prevent short circuit to occur. In order to concentrate the field lines from the Tesla high-voltage coil on one spot only, a small part of the fiber coating was stripped off using a surgical knife. Afterwards, the spark coil (BD 10ASV, EGL) was put 2-4 cm above the stripped coating part and turned on.

Result and Conclusion

It took less than 90 seconds of Tesla-spark treatment on the fiber for the hole to be accessible. The resulting hole was very smooth and there was no observable debris except for some discoloring (area around the hole was black colored). The hole diameter was around 16 μm. The result can be seen in Fig 4.4 below.

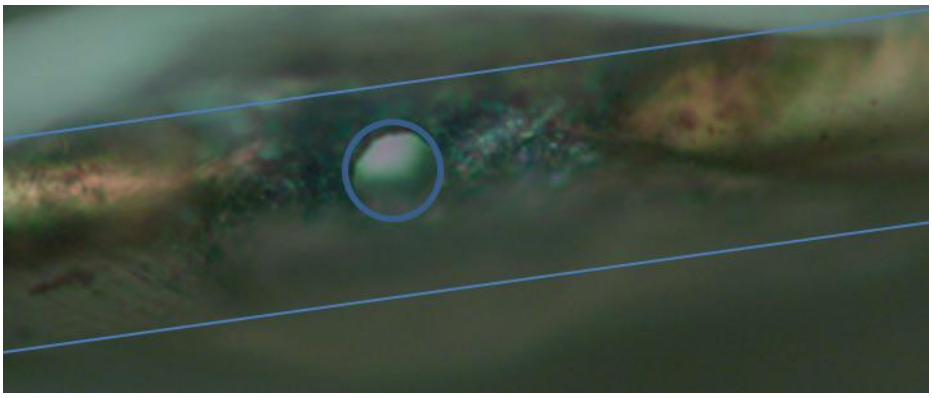

Figure 4.4: Microphotograph showing a 16 μm diameter hole (blue circle) made by the Tesla spark. The gold wire can be seen and is blue lined.

4.2 Detection

The detection of the fluorescent process is performed by the setup shown in Figure 3.10. Fluorescent dye and fluorescent beads are employed with pressure driven flow while the EGFP bacteria is detected using electro-kinetic flow.

4.2.1 Fluorescent Dye

The limit of detection for this species was investigated by the use of pressure-driven, sample-flow injection together with the fluorescent dye.

4.2.1.1 Method

The Na_2 fluorescein (F6377-100G, Sigma) was sequentially diluted with a borate buffer liquid to get the specific molar concentration. The solutions were filtered by employing a 0,22 µm membrane filter to circumvent any blockage in the fluidic system. The measurements were performed at different molar concentrations using a 1:10 dilution ratio to see if the sample still was detectable. More information regarding the insertion of the sample is given in Chapter 3.1.2 Fluidics.

4.2.1.2 Result and Conclusion

It is easily seen from the graph below, see Fig 4.5, that the sample in 1 nM fluorescent dye is barely detectable in the beginning of the time period and later on, there was mainly noise. The SNR was around 2.4, which is well below 3, indicating that it is undetectable.

The LOD for the present system (n = 6) was around 2,5 ± 0,7 nM concentration, while another research group has obtained an LOD of 50 nM using the same type of sample and buffer and at a similar pH with an optofluidic device.[40] Our results are summarized in Table 4.2.

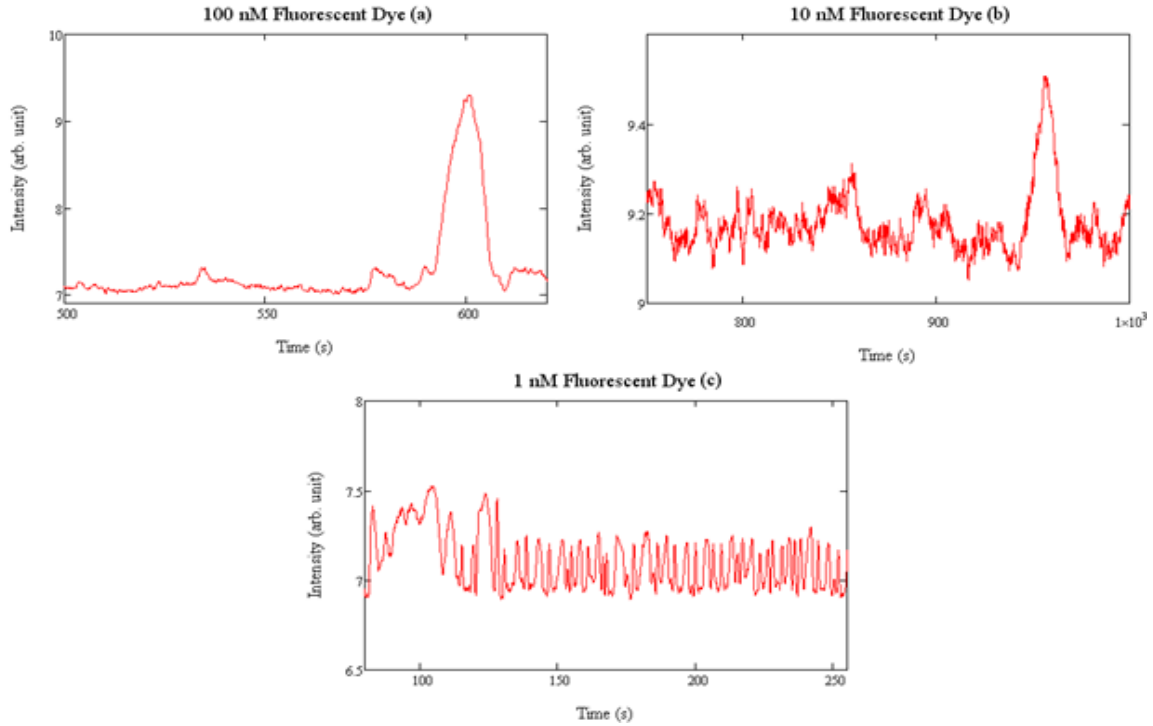

Figure 4.5: Signal intensity obtained from a pressure injected plug containing a) 100 nM, b) 10nM, and c) 1nM sodium fluorescein dye. It is seen that the 1 nM fluorescent dye is not detectable as the signal from noise is not easy to distinguish.

Concentration of Sodium fluorescein	SNR		LOD	
	Mean	Standard error	Mean	Standard error
100 nM	55	8	2 nM	0,3 nM
10 nM	7	1	3 nM	0,6 nM
1 nM	<3	NA	NA	NA

Table 4.2: The SNR and LOD (data points: n = 3) of the different concentration of sodium fluorescein is given. The standard error for 1 nM is not provided because it was not detectable hence the NA (not available). The LOD of the setup from these data will be 2,5 ± 0,7 nM.

4.2.2 Fluorescent Beads

The low limit of detection acquired for the sodium fluorescein fluorescent dye inspired us to also test the system using other analytes. Certain fluorescent beads are good candidates to be used to quantify which detection sensitivity that would be needed for identifying live cell, bacteria etc. The beads are smooth and round and with exactly the same amount of fluorescent dye in each of them.[41]

4.2.2.1 Method

The fluorescent beads were serially diluted in a borate buffer solution in order to obtain an optimal amount of beads to be detected in a suitably small time frame. The bead solution was ultrasonically dispersed in order to prevent aggregates of the beads. Then the beads were inserted into the system using pressure driven flow. The PMT voltage was set at -401 V.

4.2.2.2 Result and Conclusion

In Figure 4.6 had (a) and (b) were from the same batch but in case of a) the signal had saturated (due to the beads aggregated) but, luckily in the case of b), the signal did not saturate. However, there were too many beads and was harder to determine which bead belonged to which peak.

In case (c); the batches used in cases (a) and (b) were diluted 6 times with the borate buffer in order to reduce the concentration of the beads. The dilution made it easier to detect the individual beads as fewer beads were detected compared to cases (a) and (b) as seen in the Figure 4.6.

Several beads were detected at different intensities, which probably depended on the beads being at different flow lines. The collector efficiency of the THF was higher in the middle compared to that of the situation in which the beads were on the sides. The mean SNR with standard error (n = 5) for the fluorosphere beads was $1 \times 10^3 \pm 69$.

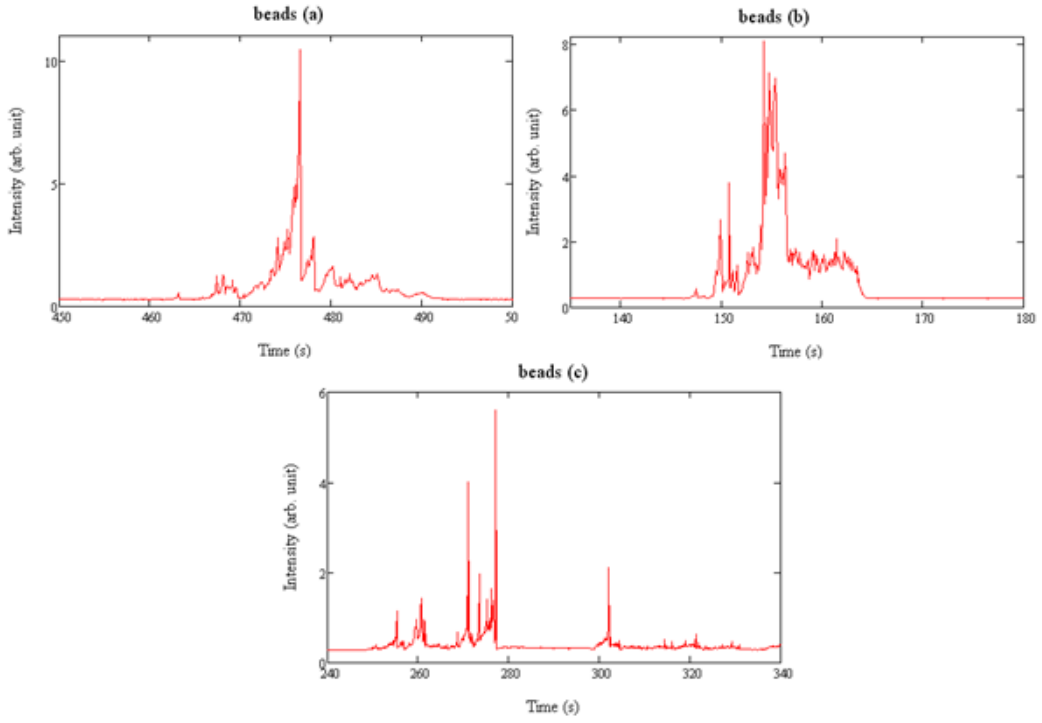

Figure 4.6: Intensity profile for beads with diameter of 4 µm using pressure driven flow. In (a), the signal is saturated due to beads aggregate. The individual beads can be seen in (b) but the beads are very close to each other. Due to this, the beads were diluted six times with borate buffer, where individual beads could be seen easily (c).

4.2.3 Live Bacterial Cell Analysis

Detection of EGFP *E-coli* bacteria has important implications in various field: chemical process monitoring, food safety, pharmaceutical production and research, environmental monitoring, homeland security and many others as well.

4.2.3.1 Method

This analysis was done using electro-kinetic flow propulsion. The enhanced GFP bacteria [One Shot® BL21(DE3) Chemically Competent E. Coli, Invitrogen],[42] prepared by the Cell Physics department at KTH, was injected into the capillary by us without using any ultrasonic treatment, as it could damage the bacteria.

4.2.3.2 Result and Conclusion

It is seen from the Figure 4.7 that there are several E-coli bacteria being detected (several peaks) within the two bumps. This pattern was recurring throughout the eight tests that were performed. There is a little difference in intensity seen in Figure 4.7 (b). The two bumps could be caused by different charge-to-size ratios (influencing the electrophoretic mobility) or bacterias being clumped together. The mean SNR from this investigation with Standard error (n = 8) is 66 ± 5.

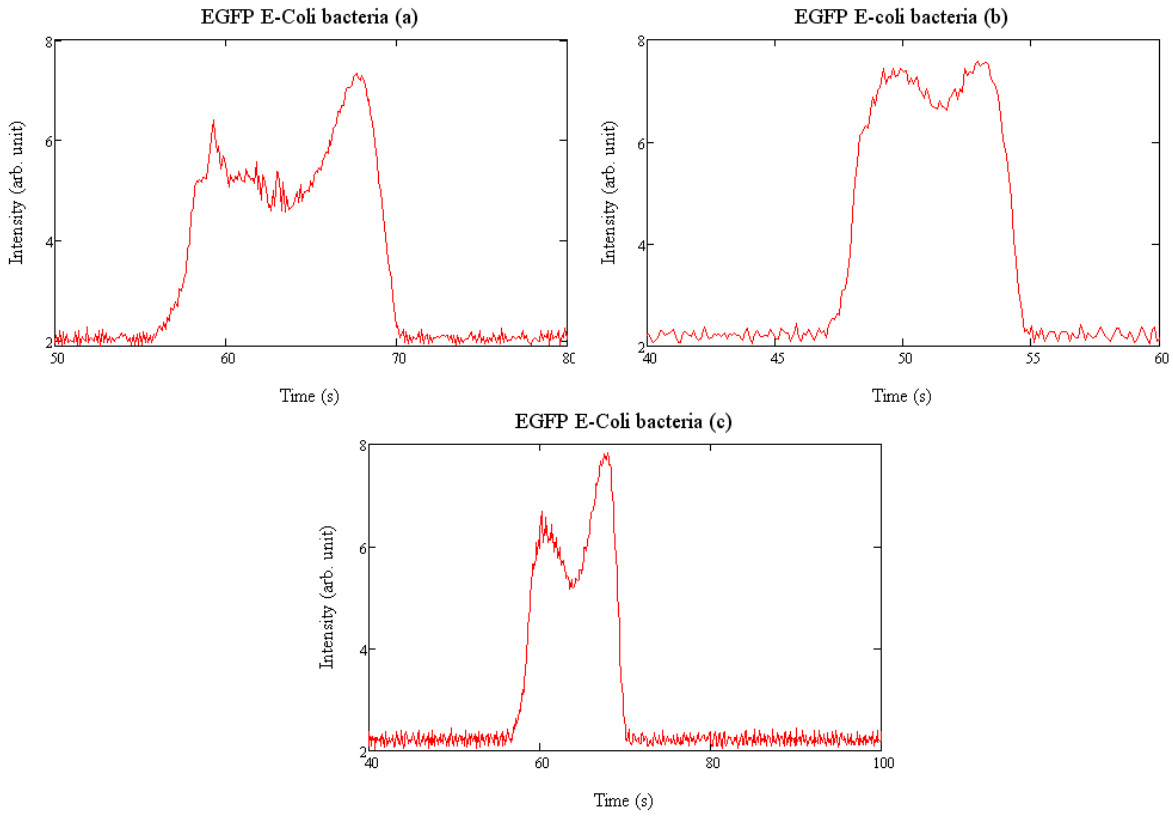

Figure 4.7: Intensity graphs for EGFP *E-coli* bacterias (BL21, DE3, Invitrogen). The (a), (b), and (c) cases were taken with the PMT voltage set at -402 V, -405 V, and -406 V respectively. This pattern of two bumps were consistent hence the test was done 8 times where the same pattern was seen except in (b) where the 2nd bump is just a little bit bigger than the first one.

4.3 Summary of the Results

4.3.1 Fabrication of a hole in fiber

The results from the different examined hole fabrication methods indicate that the Tesla spark ablation is the best method in order to create clean holes with high reproducibility. The grinding process is successful as well, but generates a significant amount of debris, which is hard to remove by ordinary cleaning methods and requires a lot of operator experience. Utilizing the current setup, the diamond saw was inconvenient to use and the reproducibility was very low. The HF etching requires a better mask adherence and, in addition, the reactive property of the HF makes it difficult and dangerous to work with. The results are summarized in Table 4.3.

Type	Preparation Time (minutes)	Time (minutes)	Additional cleaning	Comments
Tesla Spark	~10	<2	No	Cleanest but some discoloring around the hole.
HF Etching	NA	NA	Yes	HF is dangerous
Grinding	~15	~7	Yes	Debris everywhere
Diamond-blade Sawing	~10	<2	Yes	Low reproducibility

Table 4.3: Summary of the fabrication methods. Tesla spark creates better clean holes with high reproducibility.

4.3.2 Detection

The two bumps (see Figure 4.7) could be caused by different charge-to-size ratios (influencing the electrophoretic mobility) or the bacterias being clumped together. However, the reason for the different signal intensities observed between individual beads could be due to differences in their flow line positions, the signal being affected by the detection geometry where the proximity to the THF core is an important factor. Shorter distance to the core of the THF should enhance the detection signal intensity since increased fluorescence excitation as well as collection efficiency can thus be expected.

Pressure-driven flow propulsion is a convenient and reproducible technique, which works well in the system except that different analytes can flow at different velocities due to the parabolic flow profile (explained in Chapter 2.2.1). Electroosmotic flow (EOF) is easier to control under slow-speed conditions and has a beneficial velocity profile in terms of analyte band broadening. The flow in this case was sometimes obstructed probably due to clusters of beads or bacteria.

Electroosmosis and pressure-driven flow was also tried simultaneously in order to observe the movement of the beads. It was seen that the beads were going from the THF to the capillary and then back to the THF again. This can be an interesting situation as we might be able to design a setup where certain samples can go back to the THF while some can go to the capillary, which could also improve the detection if the distance is smaller from the core to the beads. The results of our detection experiments are given in Table 4.4.

Type	SNR	LOD [nM]
SMF 28 fiber (100 μM Na_2F)	$1.1x10^3 \pm 2\ x10^2$	-
Carbon coated fiber (100 μM Na_2F)	$4.2x10^3 \pm 6\ x10^2$	-
Fluorescent dye 100 nM	55±8	2±0,3
Fluorescent dye 10 nM	7±1	3±0,6
Fluorescent dye 1 nM	<3	NA
4μm Beads 6x diluted	$1x10^3 \pm 69$	-
EGFP bacteria	66±5	-

Table 4.4: Summary of detection of fluorescent dye, beads and E-coli bacteria. The carbon coated fiber is a better candidate for the setup. The limit of detection is close to 1 nM. The detection of fluorescent beads and EFGP bacteria was successful.

5 Conclusion and Future Perspectives

A fiber-based optofluidic device has been constructed that can handle and analyze fluorescent dyes, fluorescent beads, and EGFP transfected bacteria. The detection system has a high sensitivity with a limit of detection around 2,5 ± 0,7 nM for a Na_2Fluorescein solution. The Table 5.1 below sums up the objectives and research activities required to reach these objectives. The results are also given while referencing to our tables/figures.

Objective: build a fiber based optofluidic system for detection of biological sample	
Research done	**Reason/Conclusion**
Fusion	Optimal parameters for fusion between different fibers for low optical loss and keeping hole integrity. The optimum fusion parameter is provided in Table 4.1
Formation of access holes to THF	Formation of access holes is required for the flow of fluid in the system. The hole should be clean to prevent blockage. The Tesla spark was the best technique
Filters	Specific filters have to be checked to find optimum Signal-to-noise ratio. The results are shown in table Table 3.2
Selection of fiber optical cable	An ordinary single mode fiber, SMF28, introduced a lot of fluorescent background hence a better fiber was required. A Carbon coated fiber provided far less fluorescent background, hence increased the SNR by 4 times (see table Table 3.1)
Detection of fluorescent dye	Detection of different concentration of fluorescent dye will provide LOD showing performance of the setup. The LOD was around 2,5 ± 0,7 nM for Na_2Fluorescein (see Fig 4.5)
Detection of fluorescent beads	Detection of fluorescent beads acts as a simulation for biological sample in a controlled manner to see if individual beads are detected. The beads could be detected as seen in Figure 4.6
Detection of EGFP bacteria	Detection of EGFP bacteria is to demonstrate its application and to fulfill the objective. The Figure 4.7 shows the result meaning the objective was fulfilled

Table 5.1: This table shows the research which were performed with reasons and conclusions.

5.1 Future Perspectives

The present system can be improved further if the background fluorescence from the acrylate can be suppressed or decreased by improving the alignment, reducing the amount of excitation light travelling in the cladding. It was measured that around 6 mW (25% of the power input) was the power output compared to 24 mW input. This is very low and can be further improved by careful adjustment of the present and even new ancillary equipment. The alignment can, e.g., be improved by adding a V-groove fiber holder.[43] The fiber core diameter was 8 µm, which was difficult to couple to.

It is a well-known fact that it is difficult to couple light from free space into a fiber. A multimode fiber that has a large diameter should make it easier to guide in the light, which should be worth investigating, as the emitted intensity from the fluorescence is proportional to the excitation power. If we could achieve around 20 mW of excitation power, then we might be able to get 3.3 times better SNR assuming that the corresponding noise has not increased. A multimode fiber with a large

diameter will enhance factors such as mode control and the adaption of the THF to the same diameter of core.

In our experiments, some of the excitation beam was actually leaking out to the laboratory wall next to our experimental setup from the dichroic mirror. Due to this, the background fluorescence that was generated raised the noise level in the system. The utilization of some kind of beam dump should improve this situation. Furthermore, the whole system should be enclosed in a black box in order to additionally block out the noise from the surroundings.

5.1.1 Fabrication

The Tesla spark idea was shown to be a very useful microhole fabrication method as it was clean, time efficient, and cost effective. This method has not been utilized before for this purpose, making it very interesting for further investigations. Different parameters should be examined (e.g., applied voltage) to find the relationship between the integrity of the process and the size of the hole.

5.2.2 Fluid dynamics

The electroosmotic flow propulsion can be used to manipulate analytes (e.g., beads, molecules, or cells) where the flow direction can be determined by voltage control. Another interesting investigation would be to use pressure and electroosmosis simultaneously to study new possibilities for precise flow control.

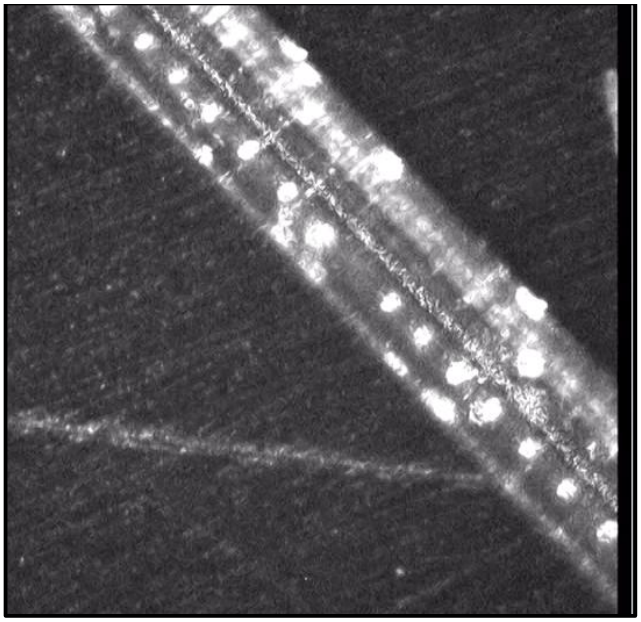

Figure 5.1: Microphotograph showing fluorescent beads flowing in a THF. The diameter of the capillary hole was 27 µm.

Our experiments revealed several interesting flow conditions where equi-positioned beads were propelled in the THF capillaries (see Figure 5.1). It should improve the possibilities for manipulating and detecting individual beads in future THF - capillary configurations (e.g., to see how two different samples react with one another in capillaries, and to study the flow profiles or even to select certain beads or analytes to specific capillaries). This is presently under investigation in our lab. We also observed that the 6 µm beads had the tendency to obstruct the flow at the capillary - THF interface. The best way to solve this issue in the future is probably to better match the THF capillary to the capillary diameter. Thermocapillary flow (by using the heat from a common lighter around the interface) was observed to be a simple way to avoid these bead flow obstructions. The beads could

be moved in the capillary by slightly heating, for example by a slow movement of the flame from the lighter. However, the flame was avoided in the bacteria experiments since this could have killed or damaged the sample. Fortunately, in this case, the obstruction of the flow was easily released by adding some overpressure. The overpressure-method worked in this case because the bacteria were much smaller than the beads and flexible enough to change a bit in shape while the beads do not change in shape at all.

5.2.3 Sample

The EGFP bacteria that we used in our experiments were used to show the system potential for real-life applications. The beads can serve as a good simulation for cells. The beads were more prone to blockage, however, compared to bacteria, which probably is due to the bacteria being smaller in size (~1 μm diameter) and their flexible characteristics. The blockage caused by the cells could be fixed by applying additional pressure while the beads required thermal inductance by a lighter. It should be interesting to try to detect other samples as well such as drugs etc., and try to select the specific fluorescent-labeled sample using some form of manipulation.

Appendix

Transmission Graphs for Different Filters

In order to pick the best filter combinations, we measured their characteristics using UV-VIS spectrophotometer (Cary 50, Varian). The graphs are shown below in Fig 6:

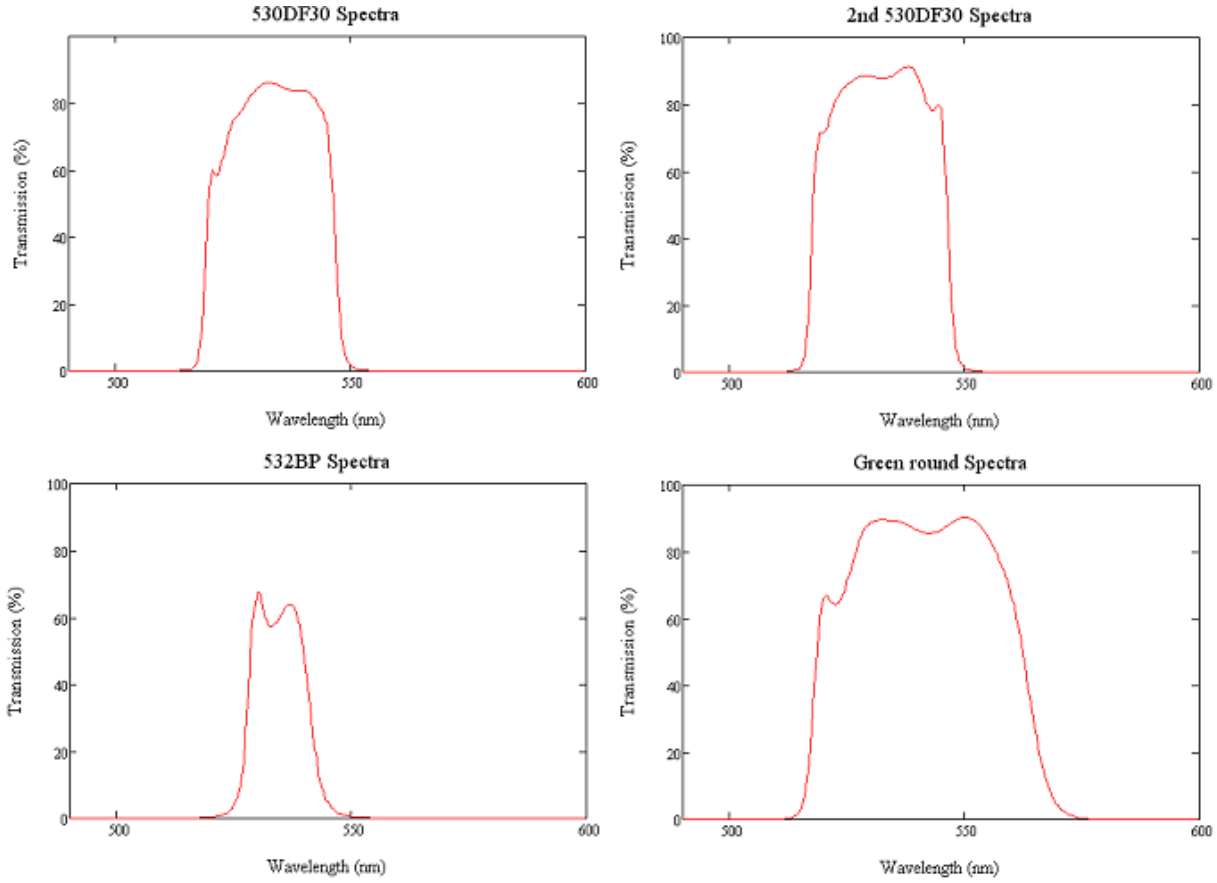

Figure 6: Measured transmission spectra for different filters using a UV-VIS spectrophotometer.

References

1. H. C. Hunt, J. S. Wilkinson, Optofluidic integration for microanalysis, Microfluid Nanofluid, 2008, **4**, 53-79.
2. http://www.laserfocusworld.com/articles/259933 Accessed 11th November 2009.
3. D. R. Reyes, D. Iossifidis, P. A. Auroux, A. Manz, Micro total analysis systems, Anal. Chem., 2002, **74**, 2623.
4. K. Hata, Y. Kichise, T. Kaneta, T. Imasaka, Hadamard transform microchip electrophoresis combined with diode laser fluorometry, Anal. Chem., 2003, **75**, 1765.
5. S. H. Lee, S. I. Cho, C. S. Lee, B. G. Kim, Y. K. Kim, Microfluidic chip for biochemical reaction and electrophoretic separation by quantitative volume control ,Sens. Actuators, 2005, **B 110**, 164.
6. J. Gao, X. F. Yin, Z. L. Fang, Integration of single cell injection, cell lysis, separation and detection of intracellular constituents on a microfluidic chip, Lab Chip, 2004, **4**, 47.
7. International Human Genome Sequencing Consortium, Initial sequencing and analysis of the human genome, Nature, 2001, **409**, 860-921.
8. J. Phil, M. Karlsson, D. T. Chiu, Microfluidic technologies in drug discovery, Drug Discovery Today, 2005, **10:20**, 1377-1383.
9. D. K. Sparacin, S. J. Spector, L. C. Kimerling, Silicon waveguide sidewall smoothing by wet chemical oxidation, J. Lightwave Technol., 2005, **23**, 2455‑2461.
10. P. J. Roberts, F. Couny, H. Sabert, Ultimate low loss of hollow-core photonic crystal fibers, Opt. Express, 2005, **13**, 236‑244.
11. K. E. Petersen, Fabrication of an integrated, planar silicon ink-jet structure, IEEE Trans. Electron. Devices, 1979, **26**, 1918.
12. A. Manz, N. Graber, H. M. Widmer, Miniaturized total chemical analysis systems: a novel concept for chemical sensing, Sens. Actuators, 1990**, B 1**, 244.
13. C. Monat, P. Domachuk, B. J. Eggleton, Integrated optofluidics: a new river of light. Nat Photonics, 2007, **1(2)**, 106-114.
14. D. Psaltis, S. R. Quake, C.H. Yang, Developing optofluidic technology through the fusion of microfluidics and optics, Nature, 2006, **442(7101)**, 381-386.
15. N.T Nguyen, S.T. Wereley, Fundamentals and Applications of Microfluidics, Artech House, 2002, ISBN 1-58053-343-4.
16. D. Li, Encyclopedia of microfluidics and nanofluidics, Springer, 2008, ISBN 978-0-387-48998-8.
17. J.C. Giddings, Unified Separation Science, 1991, ISBN: 978-0-471-52089-4.
18. V. Tandon, S. K. Bhagavatula, W. C. Nelson, B.J. Kirby, Zeta potential and electroosmotic mobility in microfluidic devices fabricated from hydrophobic polymers, Electrophoresis, 2008, **29**, 1092-1101.
19. Y. Li, L. Wang, Z. Xu, Deviations of Electroosmotic fluidic profile from electric double layer theory, Conference of nano/Micro engineered and molecular systems, 2006.
20. http://www.beckmancoulter.com/literature/Bioresearch/360643-CEPrimer1.pdf Accessed 11th November, 2009.
21. J. Tyndall, On some phenomena connected with the motion of liquids, Proc. Roy. Inst., 1854, **1**, 446.
22. N. S. Kapany, Fiber Optics. VI. Image Quality and Optical Insulation, J. Optical Society Am., 1959, **49**, 779.
23. N. S. Kapany, Fiber optics: Principles and Applications, Academic Press, San Diego, CA, 1967.
24. T. Mya, Y. Terunuma, T. Hosaka, T. Miyoshita, Ultimate low-loss single-mode fiber at 1.55 μm, Electron. Lett., 1979, **16**, 106.
25. G. P. Agrawal, Fiber-optic communication systems, 2002, ISBN 0-471-21571-6.
26. A. Mendez, T. F. Morse, Specialty optical fibers handbook, Elsevier, 2007, ISBN 978-0-12-369406-5.
27. https://www.omegafilters.com/curvo2/index.php?dyes=98&filters=&qf=&lightsources= Accessed 11th November, 2009.
28. R. T. Thompson, M. Levine, and L. Kondracki, "Component Selection for fiber-optic fluorometry," Applied Spec., 1990, **44**, 117-122.
29. J. Wilson, J. F. B. Hawkes, Optoelectronics: an introduction, 1983, ISBN 0-13-638395 5.
30. Photomultiplier Tubes R1463, R1463P, Hammamatsu specification, 1998.
31. http://probes.invitrogen.com/media/pis/mp05001.pdf Accessed 20th December, 2009.
32. Y. Matsuoka, Y. Kizuka, T. Inoue, The characteristics of laser micro drilling using a Bessel beam, Appl. Phys. A, 2006, **84**, 423-430.

33. S. Wang, W. Mies, Advanced topics on fusion splicing of Specialty fibers and devices, Proceedings of the society of photo-optical instrumentation engineers (SPIE), 2007, **6781**, 78130-78130.
34. L. Xiao, Y. Wang, C. L. Zhao, Fusion splicing photonic crystal fibers and conventional single-mode fibers: Microhole collapse effect, Journal of lightwave technology, 2007, **25**, 11.
35. P. C. H. Li, Microfluidic lab-on-a-chip for chemical and biological analysis and discovery, 2006, ISBN 978-1-57444-572-5.
36. R. Petkovsek, A. Babnik, J. Diaci, J. Mozina, Optodynamic monitoring of laser micro-drilling of glass by using a laser probe, Appl. Phys. A., 2008, **93**, 141-145.
37. K. Zimmer, R. Böhme, B. Rauschenbach, Laser etching of fused silica using an absorbed toulene layer, Appl. Phys., 2004, **A 70**, 1883-1885.
38. S. Wolf, R. N. Tauber, Silicon Processing for the VLSI Era: Volume 1 - Process Technology. Lattice Press., 1986, 531–534. ISBN 0-961672-3-7.
39. I. Steingoetter, H. Fouckhardt, Deep fused silica wet etching using an Au-free and stress-reduced sputter-deposited Cr hard mask, J. Micromech. Microeng, 2005, **15**, 2130-2135.
40. H. F. Li, J. M. Lin, R. G. Su, K. Uchiyama, T. Hobo, A compactly integrated laser-induced fluorescence detector of microchip electrophoresis, Electrophoresis, 2004, **25**, 1907.
41. http://probes.invitrogen.com/media/pis/mp05000.pdf Accessed 20th November, 2009.
42. http://products.invitrogen.com/ivgn/product/C600003?CID=Search-Product Accessed 20th December, 2009.
43. http://www.cvilaser.com/common/pdfs/HFM_HFV.pdf Accessed 20th November, 2009.